

FINAL TECHNICAL REPORT

for

National Science Foundation

Research Grant

AST 73-04908

January 1974 - August 1977

*[A 10-meter telescope for millimeter
and sub-millimeter astronomy]*

Robert B. Leighton
"

California Institute of Technology

Principal Investigator

Abstract

The design and construction of a prototype 10.4 meter, f/0.4 telescope intended for millimeter- and submillimeter-wave astronomy is described, with particular emphasis on design features, fabrication techniques, and error sources. The surface accuracy attained on a prototype dish was about 50 μm rms; on the first of four "production" dishes, about 25 μm rms; the goal for at least one of the four dishes is to be 10 μm rms or less. The reflecting surface is sheet aluminum cemented to accurately machined honeycomb panels. The 84 demountable panels are supported on a tubular steel framework which is itself disassemblable into a few easily transportable pieces. A notable feature is that the dish may be disassembled and reassembled without significant loss of accuracy and without need for later readjustment, although the means for re-adjustment are provided. The mount is of the altazimuth fork type and has an initial absolute pointing accuracy of 6 - 10" and a tracking accuracy of 1 - 2" in the absence of strong wind gusts, which degrade the tracking accuracy somewhat. The telescope, operated in an f/4.2 cassegrain mode at 230 GHz, has a system efficiency greater than 50 percent. Three such telescopes are to be installed at Owens Valley Radio Observatory and used as a millimeter-wave aperture synthesis radio interferometer. A fourth telescope, of especially high dish accuracy, is to be built and tested at OVRO and later moved to a high, dry mountain site for submillimeter infrared and radio astronomy.

CONTENTS

	Page
INTRODUCTION	1
SUMMARY OF PRINCIPAL RESULTS	9
TECHNICAL NOTES AND DISCUSSION	14
I. Dish Design and Fabrication	14
A. General description	14
B. Deflection Analysis	20
C. Accuracy and Errors	26
1. Upper Track	28
2. Slave Cart	31
3. Cutter Track	31
4. Retroreflector	36
5. Long-term Stability	36
6. Air bearing; water manometer; alignment telescope	36
7. Cutters and cutting	38
8. Panels	42
9. Panel measurement methods	42
10. Support-frame disassembly-reassembly (DA/RA)	46
11. Departures from homology; optimum panel adjustment	56
II. Mount Design and Construction	56
A. General description	56
B. Special features	57
1. Bolt-on dish attachment	57
2. Ball screw elevation drive	58
3. Epicyclic azimuth drive	58
4. Roller-thrust assemblies	60
5. Kinematic positioning	62
III. Adjustments and Tests	62
A. Axes: orthogonality and coincidence	62
B. Dish Panels	63
1. Measuring tower	63
2. Adjustment to optimum shape	65
C. Drive servos; tracking accuracy	68
1. Drive servos; steady-state and transient response	68
2. Absolute pointing accuracy; level system	75
SUMMARY AND CONCLUSION	82

INTRODUCTION

Research carried on under NSF Grant AST73-04908 was directed toward the design, construction, and testing of a prototype 10.4-meter diameter radio telescope to be used for millimeter-wave radio astronomy. If successful, the prototype instrument was also expected to serve as the first of three proposed telescopes to be deployed at Owens Valley Radio Observatory (OVRO) for aperture-synthesis radio interferometry at millimeter wavelengths. Very high goals of surface accuracy and stability of the reflector (dish) were set, with the intention of assuring essentially perfect (diffraction-limited) reflecting surfaces for wavelengths as short as 1 millimeter or even less.

The Grant extended from January 1974 until August 1977. In July 1977 a new project, AST 76-13334, was initiated to actually construct a three-telescope interferometric array at OVRO. The present report is thus both a Final Technical Report for the prototype instrument project, and an initial status report for the subsequent interferometer project. Also, certain novel design and construction features, which have not been previously described, are described here for the record.

Motivation for the project can be traced from the middle 1960's, when infrared astronomy and millimeter-wave radio astronomy entered their present especially productive periods. Scientifically, this period has seen:

- . A growing recognition of the importance of interstellar clouds, both as present sites of star formation and as regions containing numerous molecular species;
- . The discovery of astrophysical masers including OH, H₂O, and SiO in such regions;
- . Important and unexpected discoveries in solar system astronomy, from the solar interior to the outermost planets and their satellites;
- . The discovery of quasars, pulsars, and a wide range of high-energy phenomena associated with the galactic center, the central regions of many external galaxies, certain globular clusters, and certain stars.

Many of these phenomena are predominantly, or at least significantly, identified with infrared-or millimeter-wavelengths.

Technically, there has been steady improvement in i.r. detectors and radio receivers, and an extension of detection and measurement capabilities from both spectral regions toward the millimeter and submillimeter wavelengths. However, it cannot yet be said that collecting systems - telescopes - of the largest practical size and of sufficiently good surface accuracy are available to fully exploit those parts of the millimeter-wave spectrum which are transmitted by the earth's atmosphere. This is a limiting factor from the standpoint both of sensitivity and of angular resolution. A single dish of 25 m diameter, as proposed by the National Radio Astronomy Observatory, would have many times greater sensitivity than present telescopes, but still only about 10" angular resolution at its shortest design wavelength of 1 mm, insufficient to resolve many important objects. On the other hand, an interferometer comprised of two or more 10-meter dishes on a 200-meter baseline, could resolve down to 1" at 1 mm wavelength with possibly 10 or more times the presently available sensitivity. Evidently a large single-dish telescope and an interferometric array of smaller ones would provide complementary capabilities and both are needed. The present project seeks to provide the latter. Figures 1 - 3 illustrate some of the expected capabilities of an interferometer composed of 10 m dishes operating in the millimeter-wave spectral range.

The specific proposal to build a three-element interferometer of 10.4 - meter telescopes at OVRO arose from three factors:

.Much valuable experience in the design and fabrication of low-cost telescope mirrors had been gained at Caltech, starting with a NASA-sponsored 2 μ m infrared sky survey in 1965-68.

.Caltech radio astronomers were long-experienced and actively interested in radio interferometry, and the OVRO site seemed almost ideally suited for further developments toward shorter wavelengths.

.The scientific developments previously mentioned seemed to promise even more valuable results if considerably better angular resolution could be attained at very short wavelengths.

Thus in 1971 an effort was begun, under NASA support, to design and build

a low-cost prototype dish of approximately 10 meter diameter and having sufficient surface accuracy - approximately 50 μm rms - to provide diffraction-limited operation at 1 mm wavelength.

When the prototype dish was well-enough advanced toward completion that its successful performance seemed assured, a proposal to build four identical telescopes using the same dish design was submitted to NSF. As a first step toward such a possibility, a modified proposal was funded, as NSF Grant AST 7304908, which provided for the design and fabrication of a suitable mounting, and the completion of a prototype telescope. Funds for a control computer were provided by Caltech.

Figure 1: Plots of atmospheric transmission, black body spectral distribution, and dish performance degradation factors versus frequency or wavelength. Transmission curves for typical amounts of precipitable water at three observing sites, El Segundo California, Kitt Peak Arizona, and White Mountain California are shown.

These curves show that useful observations near .35 mm, .45 mm, and .6 - 1.0 mm could be made from a high, dry mountain site. The spectral distribution curve is for a 10 K black body, typical of a cool interstellar dust cloud.

The plotted function may be alternatively expressed as

$$f(\lambda, T) = \lambda F_{\lambda} / \lambda_m F_{\lambda m} = \nu F_{\nu} / \nu_m F_{\nu m} = \nu N_{\nu} / \nu_m N_{\nu m} = \lambda N_{\lambda} / \lambda_m N_{\lambda m}$$

where F_{λ} , F_{ν} , are the black body emittances and N_{λ} , N_{ν} are the photon emittances in wavelength and frequency units. For different temperatures, $f(\lambda, T)$ shifts along the wavelength axis so that its maximum point is at wavelength $\lambda_m = 3.67/T$ mm. The power emitted by a unit surface area of emissivity ϵ and temperature T , in the wavelength interval $d\lambda$ at wavelength λ is

$$dP = .736 \epsilon \sigma T^4 f(\lambda, T) d\lambda / \lambda$$

The frequencies and wavelengths of a few rotational transitions of some important molecules are shown as vertical bars with rotational quantum numbers identified.

The effects of surface irregularities in reducing the main-beam axial gain are shown for four values of surface roughness, σ , in rms micrometers.

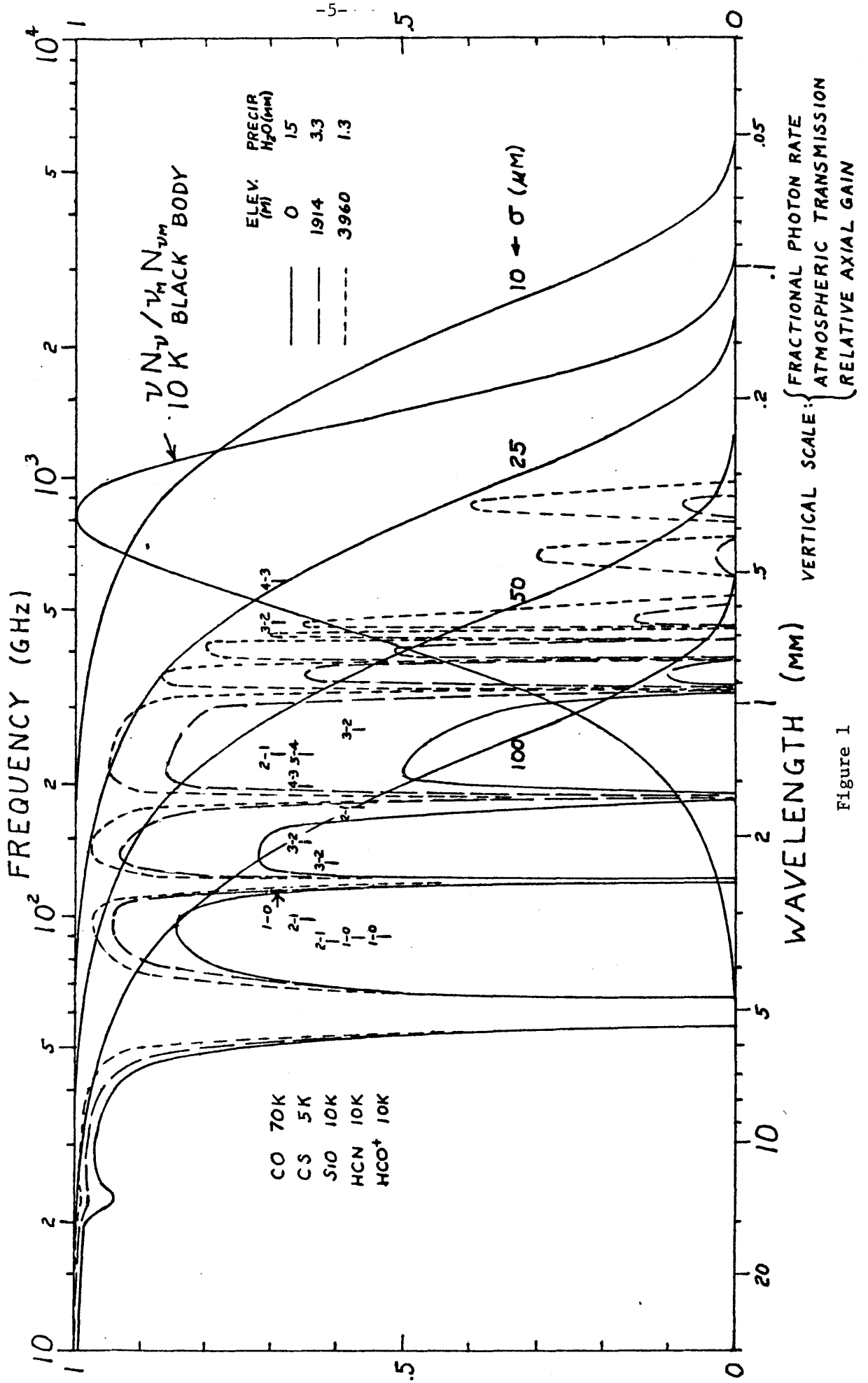


Figure 1

Figure 2: Comparison of source strengths for various solar system bodies and four of the brightest examples of cosmic millimeter-wave sources. The solar system bodies are taken as Rayleigh-Jeans black bodies at some appropriate temperature and radius, measured or estimated. For the planets, the ranges of flux densities, between the nearest (N) and farthest (F) earth distances, are shown.

The cosmic sources are: OMC-1, a molecular cloud in the Orion Nebula complex; 3C273, the brightest quasar; DR21(OH) maser source in a galactic gas-dust complex; IRC + 10216, a cool carbon star with a 600K gas-dust shell.

Also shown is the zenith atmospheric attenuation for 3.4 mm precipitable water vapor.

Two estimates of the minimum detectable flux for a 10-minute integration time with an undegraded 10-meter dish are shown: one, for a very accurate (20σ) measurement and the other, for marginal (1σ) detection. The curves suggest that all but a few of the bodies shown would be measurable with fair-to-excellent accuracy at 1 mm wavelength with such a dish.

Figure 3: (see page 8) Curves showing the interferometric resolvability as a function of baseline length. The fringe visibility parameter β is the product of source radius in radians with the projected baseline in wavelengths. The number of zeros of the fringe visibility function $V(\beta)$ for a given projected baseline (i.e., the baseline component perpendicular to the source direction) is a measure of the extent to which the source is resolved. A β - value as small as 0.2 gives a useful size measurement for an object like a planet whose general shape is known. For source mapping, the smallest resolution element is approximately the angle corresponding to the first zero of V . Thus for a 2 mm wavelength with a 200 m baseline, the resolution element would be about $1.3''$ in radius.

For comparison, the half-power beam radius of a single 10-m dish is shown for 1 mm and 2 mm wavelength, and the angular radii of various solar system objects are indicated.

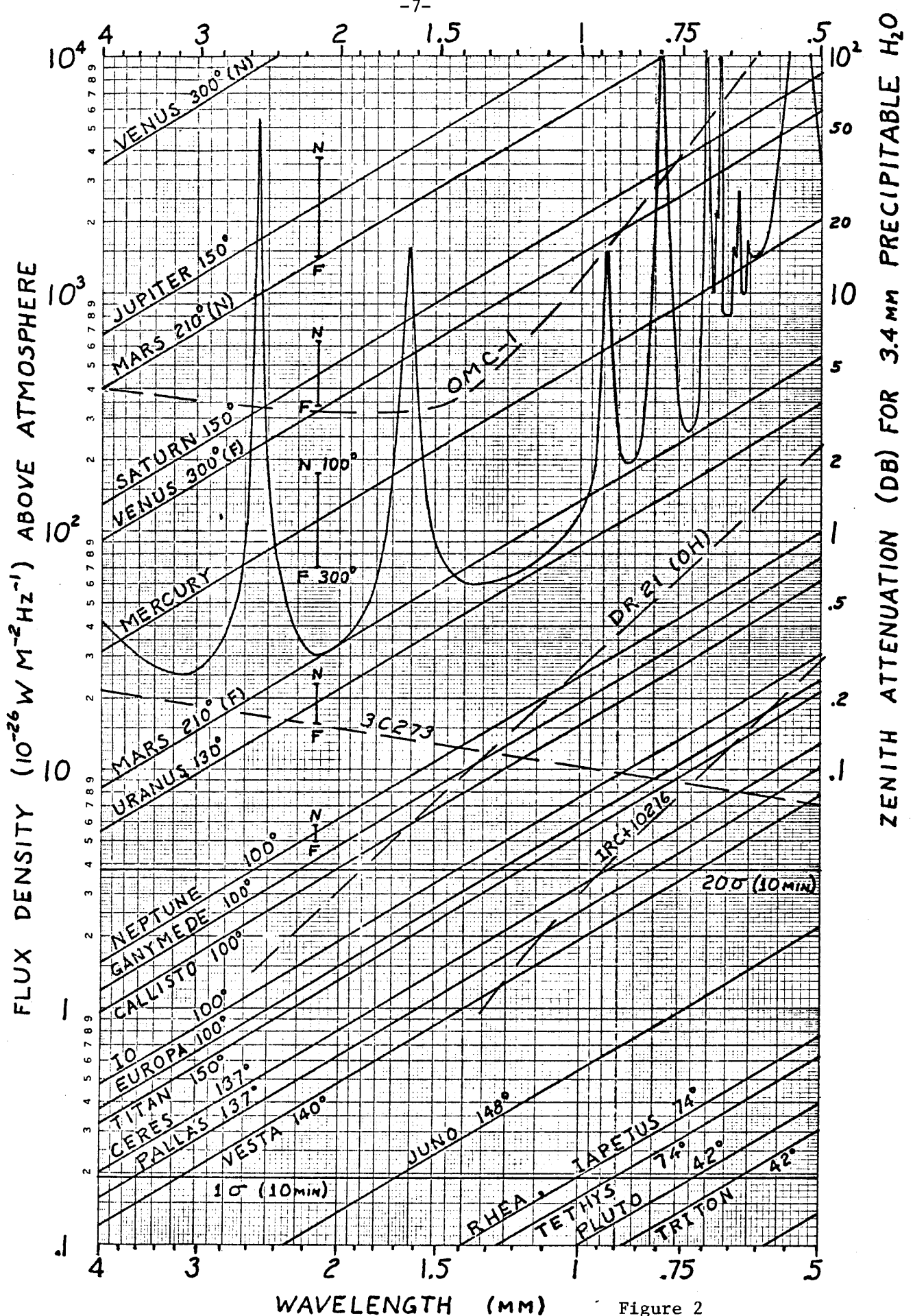


Figure 2

B (METERS) ($\lambda = 2 \text{ MM}$)

HPBW ($2 \times \text{RADIUS}$)
FOR
10M DISH
 $1 \text{ MM} \lambda$ 2MM

$\beta = \theta B / 206265 \lambda$
ZEROS OF $V = J_1(2\pi\beta) / \pi\beta$
2 3 4 6 8 10 14 18
 $\beta \rightarrow .2$
UNRESOLVED

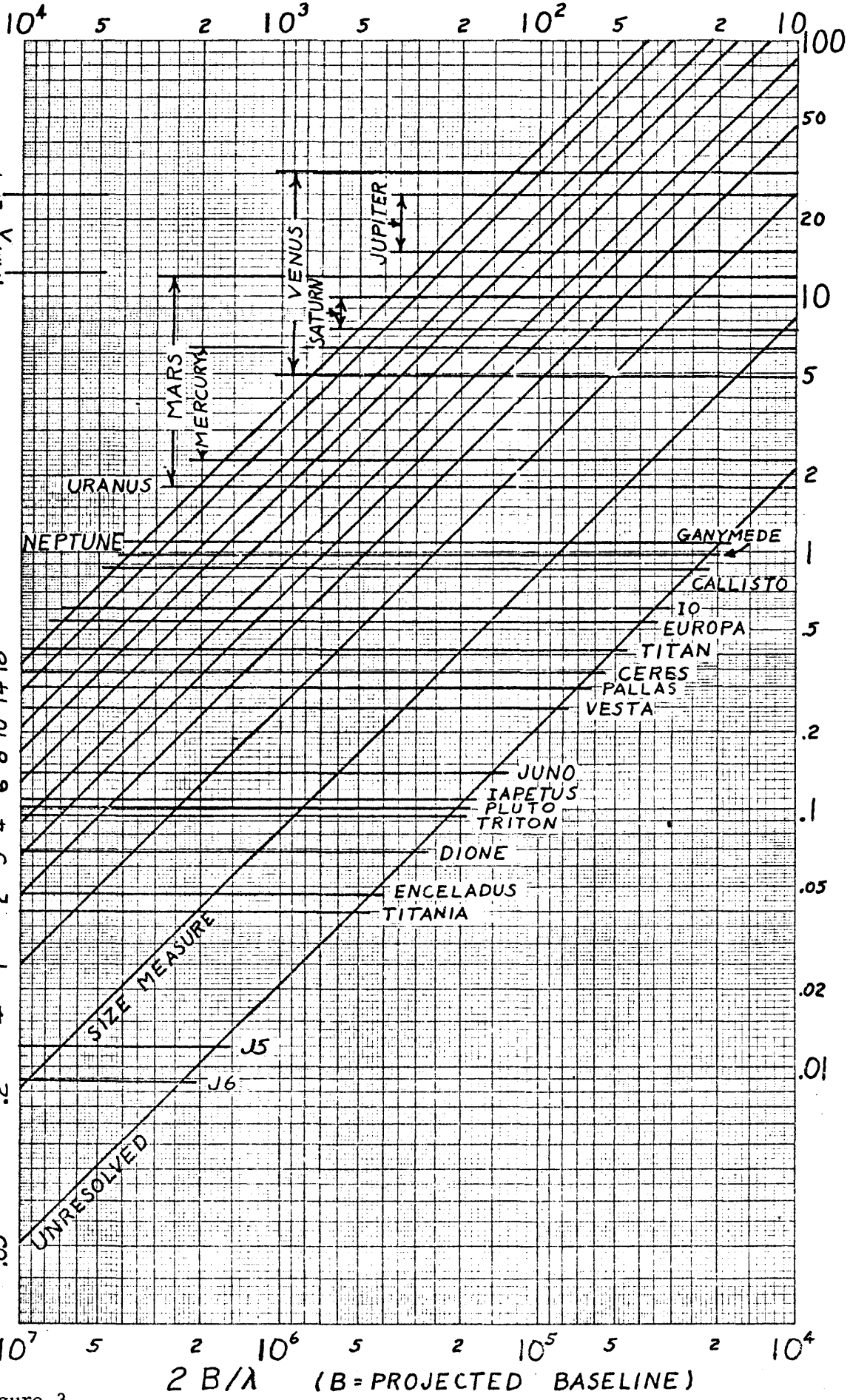


Figure 3

SUMMARY OF PRINCIPAL RESULTS

This section is a brief narrative summary of the principal results of the research project. Technical notes and discussion appear later in this report.

An initial funding increment of \$50,000 provided both for continued work on the prototype dish and for initial design of a mounting. First considered was a novel design based upon a roller drive, which promised to be relatively inexpensive because of the avoidance of large precision gears and bearings. This design was conceptually bold and exciting, but had to be discarded because of its many unproven features and because its integrity under strong winds was difficult to ensure. A more conventional altazimuth fork mount design was substituted and carried through to the design-detail stage. As first conceived, the new design used precision gears on both axes, and relatively inexpensive multi-turn shaft encoders. Later, the necessary gears were found to be unreasonably expensive, so the design was altered to use (more expensive) single-turn (20 bit) shaft encoders and less-accurate gears. In fact, large gears were entirely eliminated in the elevation drive through substitution of a ball-screw linear actuator. The net saving in this approach was estimated to be at least \$15,000 and several months' time.

Further significant savings were made in the substitution of 64-articulated cam-follower rollers for a large crossed-roller bearing.

Figure 4 shows the main features of the adopted design.

After settling on the major design features, a full set of detail drawings was prepared and put out for bids to three potential vendors. Two formal bids were received, one being considerably the more favorable. The lower bidder, L & F Industries of Los Angeles, was also known to be experienced in large telescope construction and was selected to build the prototype mounting. This activity was the principal one supported by the three subsequent funding supplements of \$205,000, \$9,200, and \$213,500 during the period Nov 1974 - Sep 1976. During this time the mount was fabricated, assembled and functionally tested at the vendor's plant, the disassembled mount was shipped to OVRO and reassembled on its concrete mounting pad, and the prototype dish was bolted

to it. By the end of 1976 all essential auxiliary instrumentation had been purchased, installed and tested. The control computer, a PDP 11/40, was installed in a large, surplus NASA instrumentation trailer situated about 250 ft. southwest of the telescope.

Pointing and tracking performance of the mount was tested using a small refracting telescope with a TV camera "eye" rigidly attached to the dish structure. Target-acquisition servo performance was evaluated visually in real time both on the TV guide telescope monitor and graphically on a computer video display. Initial imperfections in performance were readily corrected in the FORTH language software, and near-optimum performance was attained with the exception of an occasional 4-5 sec period and 4-6" amplitude "hunting" due to residual backlash in the azimuth drive. This has since been corrected by modifying the software servo loop, and tracking accuracies of about 1-2" rms are routinely observed.

Axis-alignment and other adjustment errors were evaluated by least-square fitting to pointing data for 20-30 independent bright-star sightings around the sky. Pointing accuracy of 5" - 8" rms was attained.

Initial dish performance tests were made in Feb 1977 at 1 mm wavelength using a cooled (LHe) germanium bolometer photometer. This test was made prior to the scheduled adjustment of the dish shape for optimum performance at 45° zenith angle, and during a time of marginal atmospheric transparency. No quantitative measures of overall sensitivity were obtained. A later test, made after the dish shape adjustment but also during poor observing weather, showed a marked improvement of image sharpness but again, no quantitative sensitivity values were derived.

During the period from the shipping of the prototype dish to OVRO until the tests just referred to, an improved dish called DISH 1 had been fabricated at Caltech and was ready for shipment. Certain improvements of the mount design had also been made as a result of experience with the prototype mount,

Figure 4: Side and rear views of the prototype mount (dish not shown).

Key: 1) Azimuth drive motor and speed reductor, 2) Cable wrap-up, 3) Level sensor, 4) Azimuth encoder, 5) Roller thruster ass'y., 6) Mechanical jack, 7) Tie down nut, 8) Hydraulic jack, 9) Elevation bearing ass'y., 10) Elevation encoder, 11) Platform extension, 12) Counterweight, 13) Elevation drive-ball screw, 14) Cross-roller ass'y., 15) Antenna mounting platform, 16) Transporter rails, 17) Pedestal, 18) Pedestal insulation.

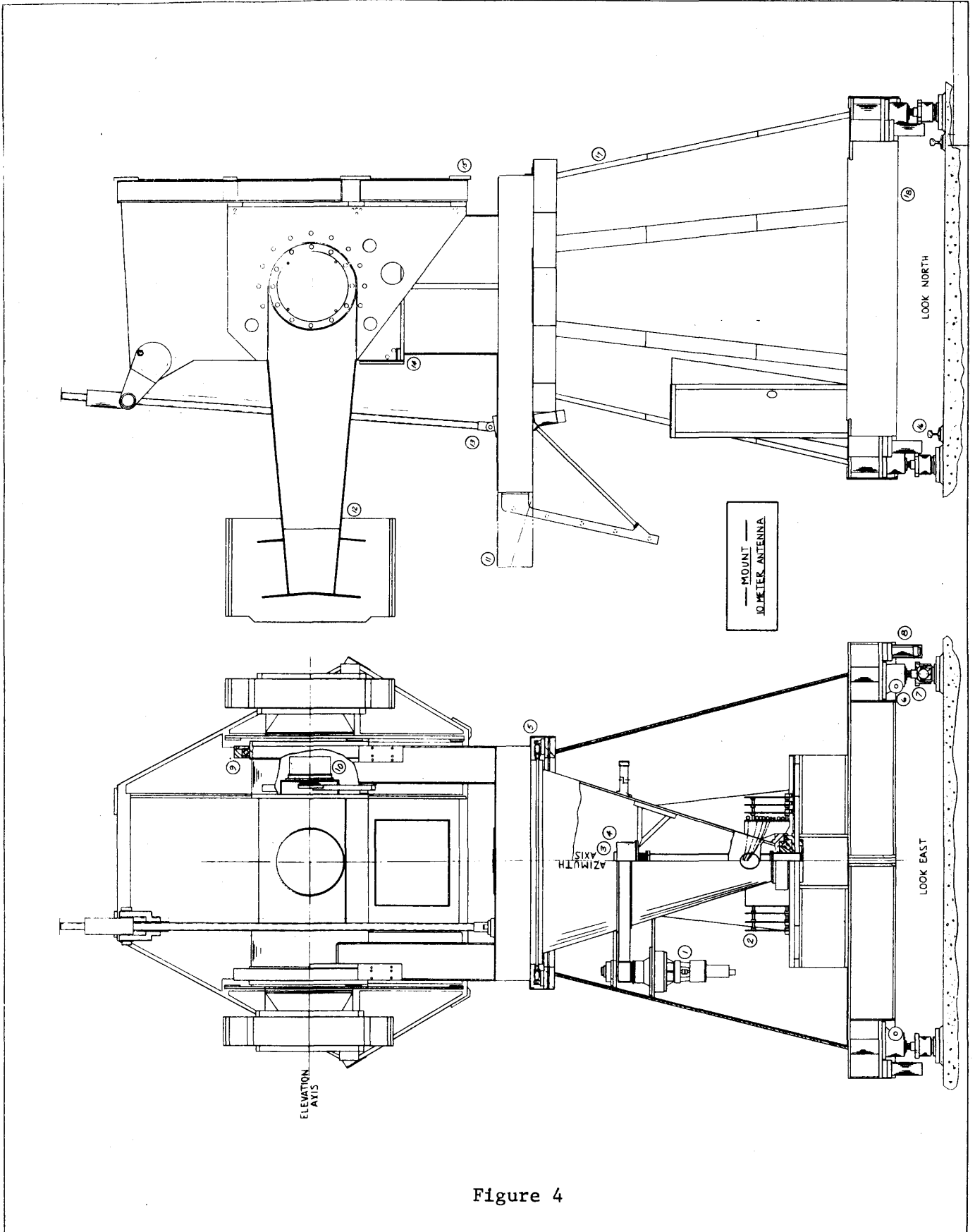


Figure 4

and it was deemed both feasible and desirable to retrofit these improvements to the prototype mount as soon as practicable. Thus, in June 1977 the prototype dish was removed from the mount and the upper part of the latter was returned to Los Angeles for reworking. In Aug 1977 the mount was reassembled and DISH 1 bolted in place.

At that time, a new capability was available at OVRO to measure the dish surface with the dish attached to the mount. By rotating the well-centered and aligned dish in azimuth, a linear transducer supported on a fixed radial frame could sense the local departures of the dish surface from an ideally constant value. In this way it was verified that the dish surface shape was indistinguishable from that which had been measured by a similar method in the laboratory (see the technical notes).

Preliminary sensitivity tests at 115 and 230 GHz (early 1978) show overall system efficiencies greater than fifty percent, and indicate that the dish figure is negligibly degraded away from the zenith.

The construction of a prototype dish and mount was well worthwhile in terms of the improvements, economies, and simplifications that were made as a result of actual experience, the validation of several unconventional design features and fabrication techniques that were used, and the improvement of surface accuracy from the initial design goal of 50 μm rms to the actually attained value of 25 μm for DISH 1 and thence to the present target value of 10 μm rms for one of four dishes to be built.

The design improvements may be briefly listed as follows:

- . Doubling of all dish strut weights to improve stiffness toward wind gusts.
- . Epoxy-cementing of most strut pin-joints to improve stiffness against gravity and wind.
- . Substitution of 24 steel "spiders" for dural ones near the dish center, to improve stiffness.
- . Substitution of notches for universal joints in panel-support rods to eliminate ~ 10 μm play.
- . Tripling of panel skin thickness to reduce panel distortions due to elastic "rebound" and thermal transients during cutting.

- . Modification of mount elevation-axis torque-tube section to provide better access to the cassegrain focus region.
- . Redesign of the initial 3-leg feed support to a 4-leg form to reduce beam blockage and to simplify fabrication and assembly.
- . Dip-priming and painting of all dish struts to eliminate inner corrosion of the hollow struts.

The principal techniques and design elements that were verified were:

- . The concept of precision dry-machining of laterally-unsupported aluminum honeycomb to provide the basic accuracy of the dish.
- . Support of dish panels on thin, laterally-flexible rods to avoid distortions due to different thermal expansions of aluminum panels and steel support structure.
- . Fine-correction of dish surface by differential-screw adjustment of support rods.
- . Routine removal and replacement of dish panels for fabrication, shipping, and any other necessary purpose without significant loss of surface precision and without need for subsequent readjustment.
- . Partial disassembly of steel support frame for shipping, and subsequent routine reassembly, without significant loss of dish surface accuracy.
- . The use of simple wooden frames to apply a predetermined convex pre-strain to each dish panel during honeycomb machining, to compensate for the later elastic "rebound" due to the deformation of the initially flat panel reflecting skins.
- . Initial setting and occasional verification of the curved cutter track by a laser interferometer, using a null property of a parabola.
- . Use of simple methods based on water-manometers to level the dish prior to machining.
- . Semi-automatic, full-scale contour-mapping of entire dish after final laboratory reassembly.

- . Selective etching of panel skins, by sodium hydroxide, to further improve surface accuracy. (Not needed except for one dish intended for submillimeter i.r. use.)
- . Interchangeability of dishes on mounts using 9-point, zero-strain bolt-down procedure.
- . Successful use of inexpensive ball-screw elevation drive in place of gears.
- . Successful use of inexpensive roller-thrust bearing assemblies in place of a large ring-bearing.
- . Real-time sensing of azimuth axis tilt using electrolytic bubble-level sensors, and direct compensation for same by the computer pointing program.

TECHNICAL NOTES AND DISCUSSION

At this time, the millimeter-wave dishes produced through the present project are probably the most accurate ones in existence, measured in terms of surface rms error per unit diameter, excluding only various smaller mirrors produced by conventional optical polishing techniques. Producing surfaces of such a size by "ordinary" machine-shop techniques to an accuracy of a fraction of a thousandth of an inch (say 15-20 μm) at first seems almost impossible if not absurd. Yet, with thorough analysis of error sources, careful design of tooling and dish structure, sufficiently sensitive and stable measurement and sensing apparatus, patient attention to adjustment procedures, and competent and dedicated professional staff, such precision is in fact attainable. As a matter of general interest and for the benefit of those who may wish to utilize some of the experience gained in the project, this section provides abbreviated notes and comments on the rationale of the design and the techniques of fabrication of the dish and mount.

I. Dish design and fabrication.

A. General Description.

The NASA-sponsored 2 μm sky survey mentioned previously was carried out

with a specially built telescope having a 1.6 m diameter, f/1.0 spincast plastic mirror. This mirror, which weighed less than 150 kg, consisted of a 5 mm thickness of slow-setting, low-viscosity epoxy resin spincast upon a machined aluminum spinning which was itself supported on a stiff sheet-aluminum egg-crate frame. Later a 3.0 m diameter, f/1.0 spincast mirror was built, using a machined polyurethane foam base and a tubular aluminum support frame. This mirror was not mounted because the larger area to be covered with epoxy led to numerous imperfections in the coating. However, the tubular support frame, whose members were easily fabricated to computer-calculated lengths, proved simple and inexpensive to construct. The latter result led to the idea of constructing an even larger dish, using the same basic scheme for the support structure but developing a more satisfactory process for producing the actual reflecting surface.

Thus a principal feature of the present dish design is that of a computer-calculated network of struts which can be readily assembled into a rigid, well defined support frame. This support structure is a steel tubular framework of parallel ("vertical") posts and connecting struts having a high degree of symmetry and redundancy, based upon a lattice of equilateral triangles in plan view (Fig. 5). The tubes have wall thicknesses chosen to optimize the stiffness for given weight. All members are fabricated to precise lengths and are assembled using close-fitting ground pins in reamed holes. This permits occasional partial disassembly and reassembly with negligible dimensional variation. At each node, all strut forces pass through a single point to avoid bending deformations which would reduce the stiffness (Fig. 6).

A lattice of 84 hexagonal-shaped aluminum honeycomb panels, each about 1.15 m in size, is supported at the triangle vertices by thin, laterally flexible high-strength steel rods having differential screw-jack adjustment capability (for fine-figuring of the surface when and if this is necessary (Fig. 7)). The upper honeycomb surface is open-celled and is machined to shape using a radially movable, template-guided high-speed cutter, and slow rotation of the mirror. During the assembly and machining, the dish is supported on a large air bearing. The time required to complete a single cut over the whole dish is about 4-8 hours.

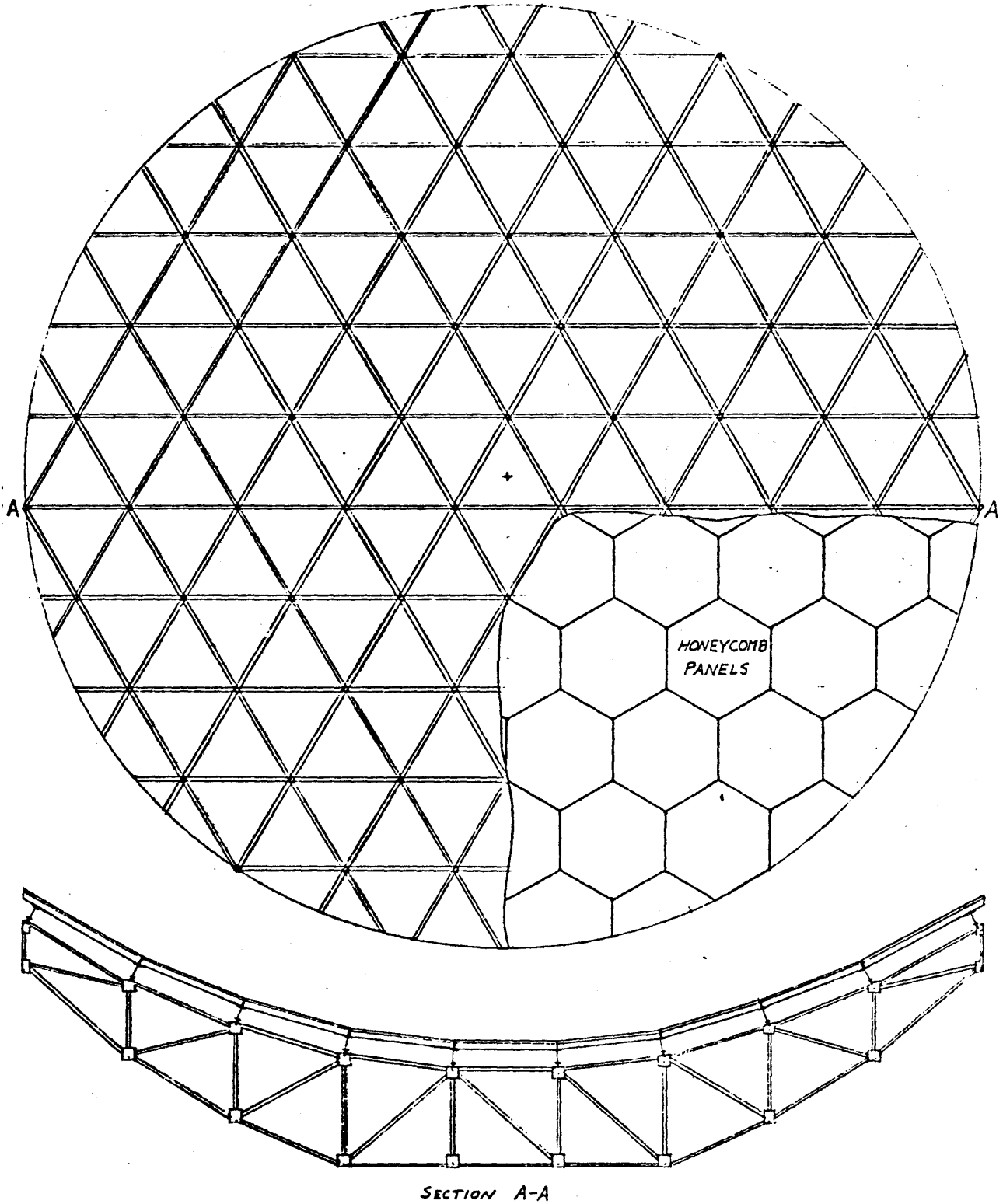


Figure 5: Schematic views of support structure and hexagonal panels

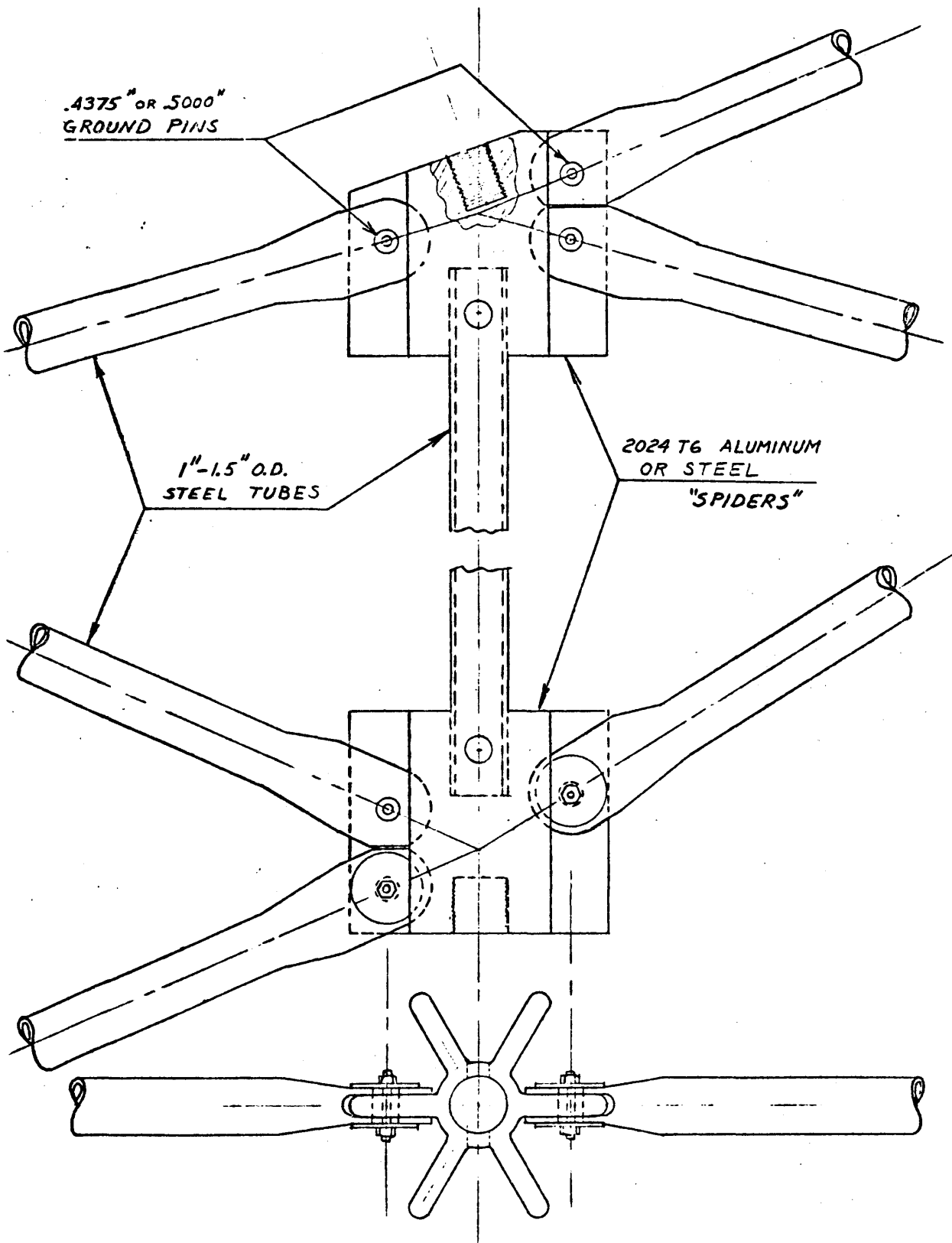


Figure 6: Schematic detail of attachment of struts, posts, and spiders at the nodal points.

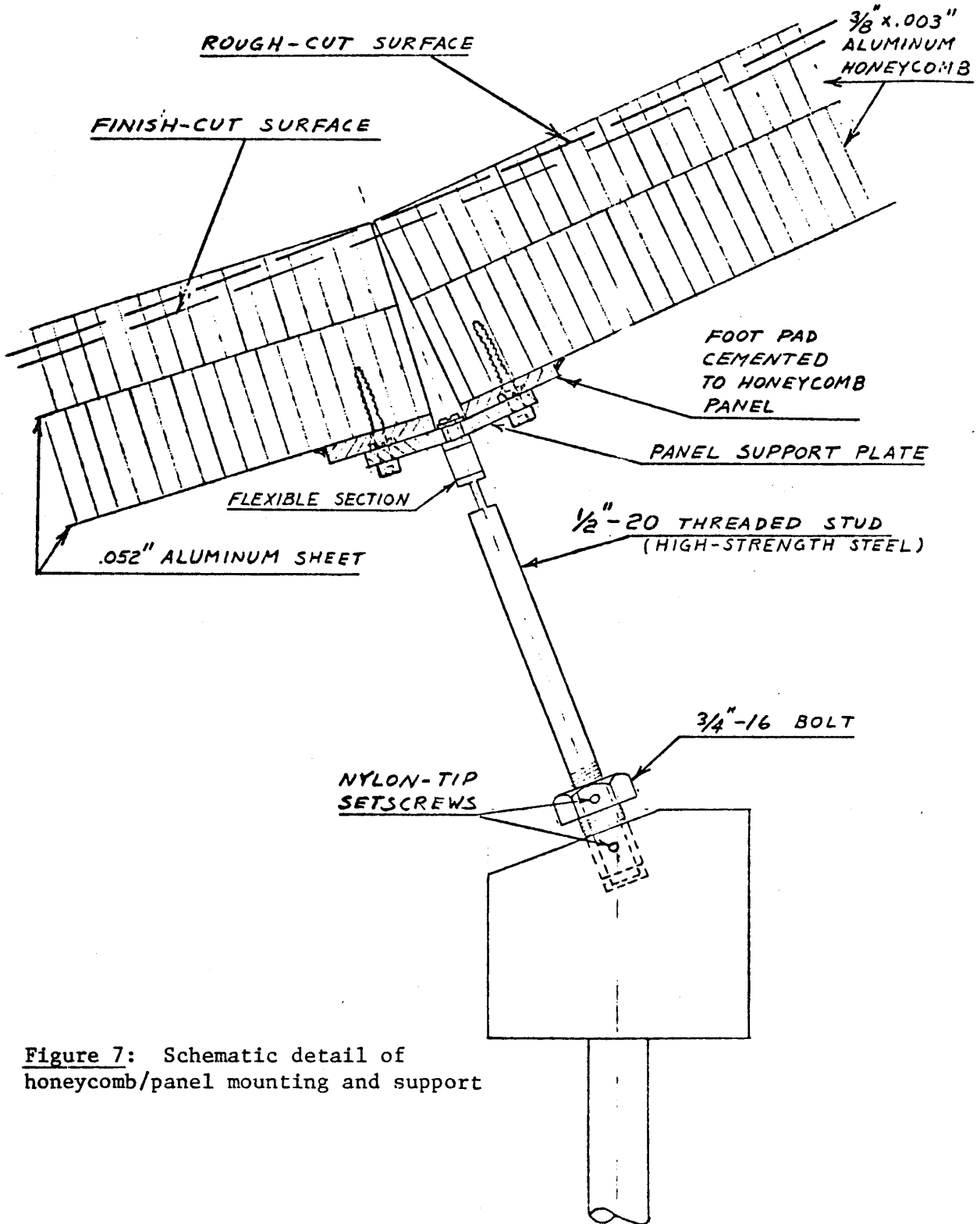


Figure 7: Schematic detail of honeycomb/panel mounting and support

The reflecting surface is 1.00 mm sheet aluminum, elastically deformed by about 0.1 atm of external pressure to mate with the machined honeycomb surface and held in place by epoxy. The machining of the honeycomb is sufficiently accurate that no further finishing of the aluminum skin is ordinarily needed.

The design goal value for surface accuracy was first set at about 25 - 50 μm . The principal potential sources of error, listed below, were carefully sought out and either directly measured or conservatively estimated. Actual construction experience easily met the necessary accuracy levels in all of the most critical areas, even allowing for error buildup by independent, multiple error sources.

- 1) Definition of a straight, level radial reference axis from which vertical offsets can be made to define the master template curve. Attained accuracy 5 μm (1974), 2 μm (1977).
- 2) Adjustment of the master template curve (cutter track). Attained accuracy 15 μm (1974), 3.5 μm (1977).
- 3) Alignment of the radial axis origin to coincide with the symmetry axis of the dish. Attained accuracy $\sim 50 \mu\text{m}$. (Necessary accuracy $\sim 500 \mu\text{m}$.)
- 4) Levelling of air-bearing (to render the rotation axis vertical). Attained accuracy $< 20 \mu\text{m}$. (Necessary accuracy $\sim 250 \mu\text{m}$.)
- 5) Non-homologous deformation of dish surface: Under symmetrical gravity loading, $\sim 10 \mu\text{m}$ (computed) out of a total deformation of about 500 μm ; Under antisymmetric (horizon-look) loading, $\sim 30 \mu\text{m}$; By resetting the panel support screws to attain a parabolic shape at 45° zenith angle, the weighted average non-homologous deformation is reduced to approximately 5 μm rms.
- 6) RMS deviation of aluminum skin thickness. Attained value $\sim 5 \mu\text{m}$. This can be improved by careful pre-selection of the skin sheet stock.
- 7) Thermal distortions due to differential solar heating of support structure members have been computer analyzed assuming plausible 30° temperature differences. Typical rms surface distortions are 10-15 μm .
- 8) The largest potential defocusing effect, if uncontrolled, is an elastic deformation of each honeycomb panel in response to the force needed to hold its

curved aluminum skin in place. This elastic response amounted to about 150 μm from center to edge of each hexagonal panel of the prototype dish. A simple device was successfully tested which pre-strains each panel by the proper amount during the machining operation, causing the cutter to remove, say, 150 μm more material from a panel center than from its edge. The elastic response then restores the panel to the proper shape when the skin is attached. This effect was thereby greatly reduced for the one half of the prototype panels on which it was tried, and was nearly eliminated for the panels of DISH 1.

These and other error sources will be discussed further later. We now consider specific factors in greater depth.

B. Deflection Analysis

The initial support-frame design was defined with the help of a simple BASIC program which evaluated the support frame deformations under symmetric (axial) loading. All listings of post and strut lengths, spider hole patterns, and other related data for parts fabrication were provided by this program. Optimization of deformation per unit frame weight was done by a version of the same program, each post and strut being considered individually. For the actual design, all struts at a given (hexagonal) "radius" from the axis were assigned the same wall thickness, a commercial value lying close to the average for that radius. Four such "weight classes" were used for struts and four for the axial posts. Table I gives the post and strut cross-section dimensions for DISH 1 (approximately twice the areas of the prototype members).

Up to this point the elastic properties of the pinned joints, flattened strut-ends, and aluminum spiders had been ignored. For detailed deflection and stress analysis, a more general FORTRAN program was written, which permitted the above effects as well as actual looseness in the pin joints, thermal expansion effects, and arbitrary external forces such as wind loads, feed-support loads, etc. to be treated.

The pin-joints and spider elastic properties were characterized experimentally by testing actual such joints in a testing machine, comparing the extensibility of a specimen composed of three such joints in series with that of the same total length of strut material. Each combination of strut cross-section, spider fin thickness, and pin size was so modeled, and the corresponding end effects, expressed as the lengths of strut material whose extensibilities

TABLE I

POST AND STRUT TUBING DIAMETERS AND WALL THICKNESSES (INCHES)

WEIGHT CLASS	POSTS		STRUTS	
	DIA.	WALL	DIA.	WALL
1	1.50	Solid	1.50	.281
2	1.25	Solid	1.50	.281
3	1.12	.188	1.25	.188
4	1.00	.083	1.00	.120

DISH 1 WEIGHTS:
(Nominal)

Support Frame	3130 kg
Panels	1380
Feed Support	<u>225</u>
Total	4735 kg

would account for 1/3 of the observed differences between the jointed and unjointed specimens, were evaluated. In general, the additional deformation of one strut end, pin, and spider fin was equivalent to the theoretical deformation of from 10 to 25 cm length of strut. These tests clearly revealed the effects of the pin joint itself and of the substitution of more extensible aluminum fins for a corresponding length of steel strut. Thus it was found desirable to use steel spiders rather than aluminum ones in the innermost 24 vertices, to increase the stiffness.

The same series of tests also established that the yield-and ultimate strengths of the pin joints were far greater than any conceivable operational or environmental situation would require.

The program solved for the x, y, and z components of the displacement of each vertex from its unstressed position by an iterative method: A "stiffness factor" for each vertex was calculated for the case where all vertices except that one were held fixed, and the latter vertex was displaced in the x, y, or z direction. Starting with given vertex displacements and applied forces (usually including weights of struts and dish panels), the unbalanced force at each vertex was evaluated by elementary elasticity theory ($F = YA\Delta\ell/\ell$). Each vertex was then assumed to move in the direction of the unbalanced force by an amount equal to the force divided by the vertex stiffness factor. The cycle was then iterated until the maximum unbalanced force component on any vertex fell below, say, 1 Nt, and the rms unbalanced force component fell below 1/3 Nt. The number of iterations needed to accomplish this was generally 500 - 1500. Convergence was materially enhanced by sensing the trend of the incremental displacements, extrapolating to guessed convergence values, and reiterating from these new starting points. Figure 8 shows deflection "maps" of the upper vertices for the case of symmetrical loading.

Many different stress and displacement calculations were made using this program, including

Gravity deflections for various dish orientations.

Comparative zenith-to-horizon shape differences for various dish support schemes.

Deflections and member stresses for various wind loads.

VERTEX DISPLACEMENTS IN 1/10-MIL UNITS FOR TILT 0.0 DEGR 1 VERTEX, 1 COMPONENT

(76)	(77)	(78)	(79)	(80)	(81)	(82)	(83)	(84)	(85)	(86)	(87)
-68							-70				
(1)	(2)	(3)	(4)	(5)	(6)	(7)	(8)	(9)	(10)	(11)	(12)
-40	-54	-55	-56	-55	-43						
(108)	(109)	(110)	(111)	(112)	(113)	(114)	(115)	(116)	(117)	(118)	(119)
-26	-30	-30	-34	-37	-35	-31	-33	-31			
(107)	(108)	(109)	(110)	(111)	(112)	(113)	(114)	(115)	(116)	(117)	(118)
-16	-20	-19	-18	-22	-22	-19	-20	-22	-23		
(106)	(107)	(108)	(109)	(110)	(111)	(112)	(113)	(114)	(115)	(116)	(117)
-9	-7	-6	-6	-7	-6	-7	-6	-7	-9	-10	
(31)	(32)	(33)	(34)	(35)	(36)	(37)	(38)	(39)	(40)	(41)	(42)
-2	0	0	0	-1	-1	0	0	0	0	3	
(105)	(106)	(107)	(108)	(109)	(110)	(111)	(112)	(113)	(114)	(115)	(116)
8	7	5	4	3	2	3	4	5	6	7	
(104)	(105)	(106)	(107)	(108)	(109)	(110)	(111)	(112)	(113)	(114)	(115)
21	14	12	9	9	9	9	12	14	19		
(102)	(103)	(104)	(105)	(106)	(107)	(108)	(109)	(110)	(111)	(112)	(113)
33	31	25	21	25	21	25	32	38			
(100)	(101)	(102)	(103)	(104)	(105)	(106)	(107)	(108)	(109)	(110)	(111)
39	2	33	34	34	34	34	43	43			
(98)	(99)	(100)	(101)	(102)	(103)	(104)	(105)	(106)	(107)	(108)	(109)
5	5	49	46	47	47	51	54				
(97)	(98)	(99)	(100)	(101)	(102)	(103)	(104)	(105)	(106)	(107)	(108)
43	43	50	44								

Figure 8a: Deflection components of the upper vertices of the dish support frame for axial loading (zenith-look direction). The x-and-y directions are indicated in the figure. The z direction is in the upward vertical direction (see also figures 8b and 8c).

VERTEX DISPLACEMENTS IN 1/10-MIL UNITS FOR TILT										0.0 DEG	1 VERTEX, 2 COMPONENT	
	(76)	(78)	(80)	(82)								
	-20	-R	0	7								
	(1)									(6)		
	-16	-13	-5	3	12					15		
(10A)	-14 (7)									(84)		
	-16	-9	-5	0	6	10				(13)	15	
				F								
(107)	-14(14)									(85)		
	-17	-10	-8	-1	2	3				(21)	16	
106)										(86)		
-21(22)										(30)	24	
-27	-18	-11	-5	0	5	11					28	
										(40)		
	-22	-14	-8	-2	1	8				14	23	30
		F			***->Y					F		
					V							
5)(41)					V						(49)	(87)
0 -37	-21	-11	-5	0	3	12				22	38	51
				X								
(84)										(89)		
41	(50)									(57)	45	
	-32	-18	-9	-2	4	10				19	34	
(102)	(5A)									(64)	(91)	
-81	-25	-11	-3	0	4	12				26	43	
				F								
(100)	(65)									(70)	(93)	
-33	-22	-10	-3	4	10					22	34	
	(9A)									(94)		
	-27									27		
		(71)								(75)		
		-15	-9	0	9					15		
		(97)								(95)		
		-5	0	5								

Figure 8b

VERTEX DISPLACEMENTS IN 1/10-MIL UNITS FOR TILT 0.0 DEG 1 VERTEX, 3 COMPONENT

	(76)	(77)	(78)	(79)	(80)	(81)	(82)	(83)	(84)
	-171							-173	
	(11)							(6)	
	-133	-139	-141	-145	-141	-135			
	(108)							(84)	
	-127	(7)						(13)	-129
	-109	-98	-93	-96	-93	-99		-110	
				F					
	(107)							(85)	
	-101	(14)						(21)	-105
	-95	-73	-57	-50	-48	-56	-74	-96	
	(106)							(86)	
	-107	(22)						(30)	-109
	-88	-60	-31	-7	-3	-6	-31	-61	-89
	(31)							(40)	
	-95	-70	-39	-6	0	0	-6	-39	-71
			F					F	
					**=>Y				
					V				
					V				
	(105)	(41)			0	-3	-30	-61	(49)
	-123	-96	-61	-30	-3	-30	-61	-97	-124
					X				
	(104)							(89)	
	-121	(50)						(57)	-124
	-96	-60	-30	-7	-7	-30	-61	-97	
	(102)	(58)						(64)	(91)
	-149	-113	-78	-57	-51	-58	-79	-114	-152
					F				
	(100)	(65)						(70)	(93)
	-180	-122	-99	-89	-91	-101	-124	-144	
		(98)						(94)	
		-147						-150	
			(71)					(75)	
			-142	-126	-125	-128	-144		
			(97)					(95)	
			-142	-137	-143				

Figure 8c

Comparative effects of different amounts of pin-joint play.

Thermal distortions due to solar illumination at various angles, including shadowing effects of panels.

Internal stresses due to random, gaussian strut length errors.

Comparative deflections with and without lap-shear epoxy at strut-spider pin joints.

C. Accuracy and errors

The arrangement of the air bearing, dish structure, template girder, and laser interferometer system is shown in Figure 9. The objective is to adjust the system so that the path followed by the cutter edge as the cutter cart C moves along the template track T_C is a parabola having a vertical axis and a known focus F, and so that the dish structure rotates on the air bearing B about a vertical axis passing through F. The interferometer is arranged to yield a constant reading if the path of the mirror M is parabolic and the cat's-eye retroreflector apex R_m is at the focus: The laser beam LB is directed horizontally so as to go through an entrance aperture on the slave cart S cleanly for any position of the cart along the upper track T_D . The beam first encounters the reference-arm beam splitter R_R on the cart, and the transmitted part is bent 90° downward by a pentaprism P, also fixed on the cart. The vertically moving rays next strike the plane mirror M which is situated precisely where the cutter edge will later be during the final cut on the honeycomb. The beam is reflected diagonally upward to the retroreflector R_M where it is laterally displaced by about 12 mm and thence returned to the laser L along a path paralleling the outgoing one.

Figure 9: Schematic diagram of air bearing, dish structure, template girder, and laser interferometer system. See text for explanation. Key: B, B upper and lower air bearing rings; F, focus of parabola; L, laser head; LB, laser beam; R_R , reference-arm retroreflector; P, pentaprism; M, plane mirror; R_M , measuring arm retroreflector; T_D , upper (directrix) track; T_C , lower (cutter template) track; C, cutter cart; S, slave cart; MA, manometer; MI, 50x viewing microscope; O, observer; MT, Manometer tubing; AT, alignment telescope; SR, spherical reflector; FB, flashlight bulb; CF, cam-follower.

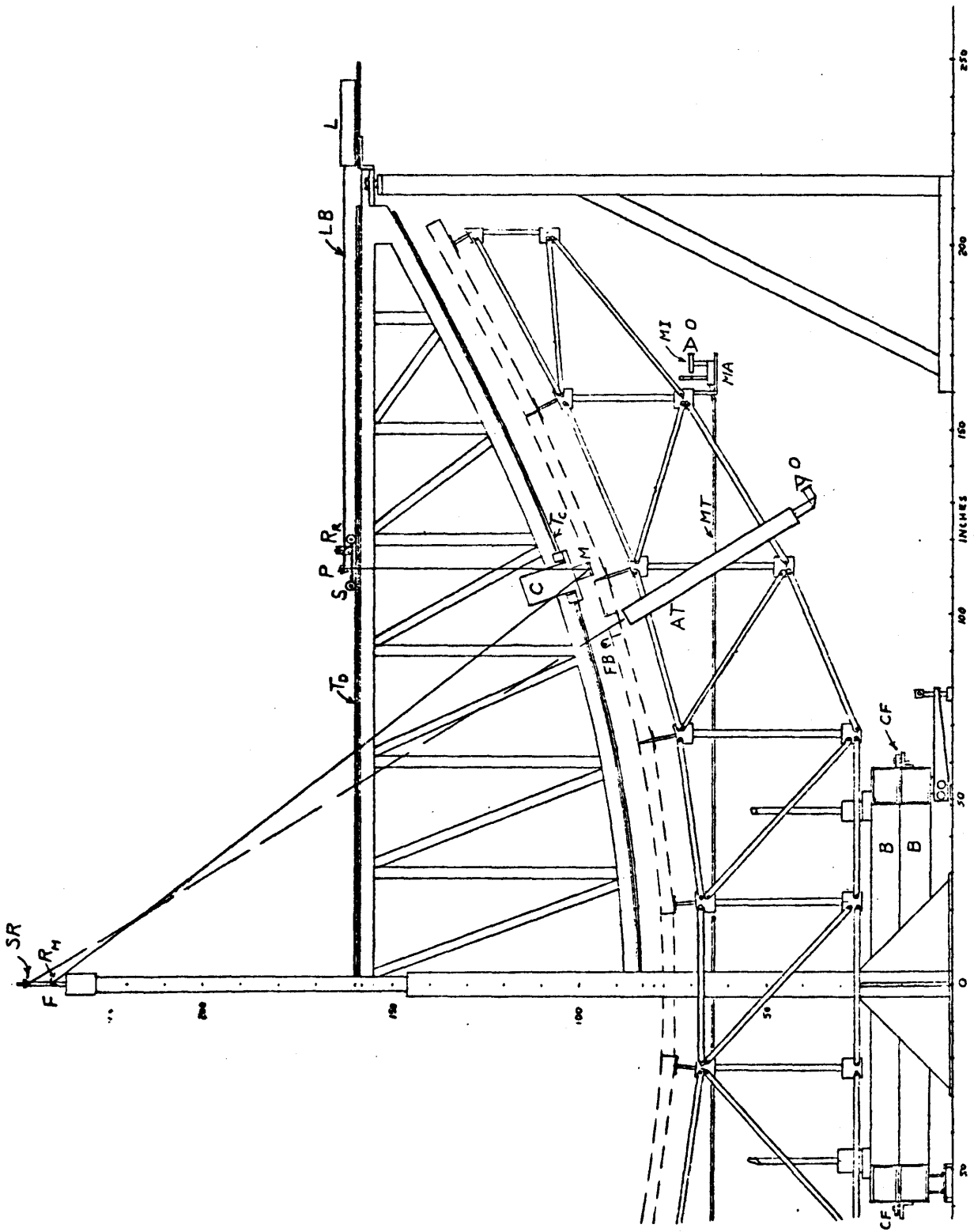


Figure 9

The slave cart S (Fig. 10) carries photocells C,C, which detect whether the return beam is high or low and this signal is used to servo-control the motor-driven cart so as to center the return beam. (The optical path length is first-order invariant to small errors in the cart position, so this is not a difficult control problem.)

1. Upper track

The upper track T_D serves as "directrix" for the parabola, and as such it must be straight and level. This is accomplished as follows: (Fig. 10)

An aluminum trough 5 cm wide x 2.5 cm deep is mounted just below one edge of the upper track, in such a way that it can be moved laterally about 3 cm either to pass the downward-moving laser beam or to intercept it near the trough centerline. This trough is filled with light oil to a depth of 8-10 mm, and a modified monocular microscope is so placed on the slave cart S as to be able to focus on the oil surface. A small beam-splitter cube is mounted in the barrel above the objective lens so as to intercept the horizontal laser beam LB and direct part of it downward through the objective. If the microscope is focused on the oil surface, the small fraction of the (sharply convergent) laser light that is reflected from the oil retraces its path back up through the objective, emerging as a nearly-parallel bundle above it. A portion of this bundle traverses the splitter cube and can be seen visually through the eyepiece. By suitably adjusting the microscope focus (i.e. height), this spot can be brought to a sharp focus. The size of the focal spot is a sensitive function of height, and as little as 2-4 μm of height difference can be consistently resolved. In order to tell whether the microscope is too high or too low, a weak cylinder (spectacle) lens, with cylinder axis at 45° to the vertical, is mounted where the laser beam enters the splitter cube. This produces two astigmatic line foci, and the orientation of the intermediate elliptical images provide the necessary directional information. A linear transducer T attached to the microscope barrel sensitively measures the height of the cart with respect to the microscope.

Figure 10: Slave cart detail (schematic). Key: S, slave cart body; LB, laser beam; R_R , reference-arm retroreflector; P, pentaprism; C,C photocell beam detectors; M, drive motor; T, linear transducer; O, oil-filled trough; T_D , top track; G, template girder. In the upper figure, the pentaprism and retroreflector have been replaced by a high-power microscope and beamsplitter, and the level reference oil-trough has been slid laterally into place. This configuration is used to adjust the upper track for straightness and horizontal level.

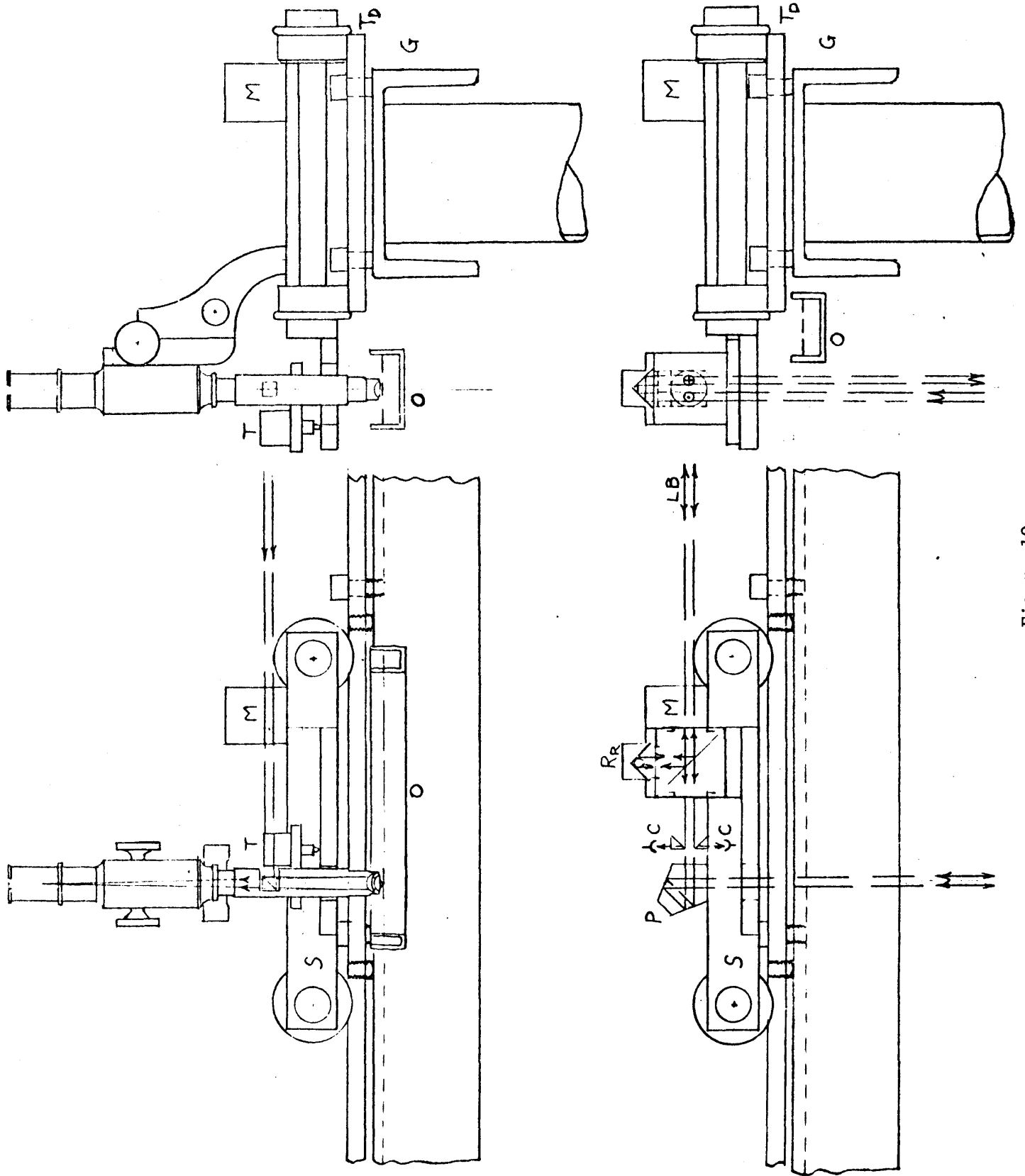


Figure 10

The oil trough provides a convenient, reliable level reference, and the height variations of the slave cart are readily measured to within a few μm rms with it.

For many purposes the oil-trough leveling would suffice. But it is also important, for satisfactory interferometry, that the upper track be uniformly level in the lateral direction also. Thus a sensitive water-manometer level (or other similar device) is used to evaluate and correct the cross-level variations.

Finally, the upper track should be as smooth as possible in its shape. The oil-trough level treats each measurement as independent. Another device, which senses local smoothness (absence of curvature) is also helpful, particularly in monitoring the process of height adjustment of the track. The device measures the sagitta of an appropriate section of track, and is called a sagmeter. In its simplest form, it consists of two fixed, smooth "feet" which rest on the track some distance apart, and a sensitive dial indicator (or electrical transducer) which senses the track height at the midpoint between the feet. (It is essentially a "linear spherometer".) If h_1 , h_2 , and h_3 are the respective heights of the three points of the track, h_2 being the center point, the sagmeter measures $s = h_2 - \frac{1}{2}(h_1 + h_3)$, i.e., the height at the center relative to the average of the two ends. (This assumes that the meter is set to zero on a truly flat surface.)

For historical reasons, the arrangement of adjustment screws on the upper track is such that a rather more elaborate sagmeter is in fact useful. First, one wants to measure both sides of the 20-cm wide track at the same time, so two parallel sagmeters are needed. Then, it is necessary to measure the track height not only at the center point but wherever an adjustment point exists. For the actual upper track, the basic spacing of the push-pull adjustment screws is some 25 cm, so the basic sagmeter length is 50 cm. (Each foot must rest on the track at an adjustment point, so that the feet will remain fixed when the intermediate point is adjusted.) The 25-cm screw spacing was found to be too coarse to permit sufficiently precise adjustment, so additional screws were later added. The original screw locations are called stations, and there are 21 of these along each edge of the track. It was found that placing dial indicators on the sagmeter

not only at the station midway between the two reference stations but also at the "half-station" and "quarter-station" points aided in the adjustment procedure.

Thus the upper-track sagmeter carries ten similar dial indicators registering $2.5 \mu\text{m}$ (0.0001 in) per division. These are all set to zero on a granite surface plate to within approximately $1 \mu\text{m}$.

From the oil-trough leveling and cross-leveling data, nominal absolute track height corrections at the full-station points are derived. Those corrections are applied by centering the sagmeter at a full-station point and monitoring the adjustment there with the dial indicator. Corrections less than $1 \mu\text{m}$ are not made. At the track-end stations (Nos. 0 and 20), an obvious variation of the procedure is used.

Upon completing this procedure, the sagmeter indicators are zeroed on the surface plate and the track is gone over again, this time with the aim of using all adjustment screws to reduce all dial readings to as near zero as possible. With experience, this is easy to do and results in a noticeable improvement in the local smoothness of the track. (Note that one only adjusts screws between the sagmeter feet except when the 0th or 20th stations are involved.

For DISH 1, three or four iterations of the above procedure resulted in a residual departure of $5 \mu\text{m}$ rms from a best-fit parabolic curve. (The linear term can be removed by a suitable readjustment of level, and the other terms do not matter.)

2. Slave cart.

Periodic errors of about $5 \mu\text{m}$ exist in measurements involving the use of the motor-driven, wheeled slave cart due to eccentricities in its four wheels. Pending further attempts to remove the eccentricities, these errors are minimized by averaging two successive runs with the wheels shifted 180° in phase between them.

3. Cutter track.

Like the upper track, the curved cutter track is a length of 1.27 cm x 20.3 cm (.500 in x 8.000 in) ground cold-rolled steel, supported by two rows of equally-spaced push-pull adjustment screws. Here the initial screw spacing was 15 cm, but experience again showed that a finer spacing would

be better. Another set of screws was provided, spaced halfway between the existing set, after DISH 1 was finished.

The cutter cart rests on three nylon footpads, two of which are spaced 30.5 cm (12.00 in) apart along the cutter-motor side of the track, and the third is on the opposite side of the track across from the outermost one of the first two pads. The cart is motor driven along the track at an adjustable speed by a gear-and-rack cog system.

Three kinds of measurements are used in the adjustment of the cutter track: 1) The lateral offset of the returning laser beam with respect to the outgoing beam, 2) the laser interferometer measurement of beam-path fluctuations, and 3) sagmeter measurements of local track curvature.

The lateral beam offset is important mostly because the interferometer can tolerate only about 2-3 mm of beam misalignment without dropping out of "lock". With the cutter cart moving slowly up the track, the beam offset is observed visually at each station and half station of the cutter track. These measures are later converted into equivalent lateral track "tilt" and incorporated into the next readjustment.

The laser interferometer record is straightforward to obtain and interpret. The path-length signal is recorded on a strip-chart recorder at a longitudinal scale which gives adequate resolution along the track, and at a lateral scale of about 125 μm of track displacement (250 μm of beam path length) per full chart width. "Pips" are automatically recorded at each full station. (See Fig. 11.)

Figure 11; Half-size reproduction of the final laser interferometer record prior to cutting DISH 2. (The reduced-scale chart record was cut and pasted onto a single page.) The record begins at station 3.25 near the innermost panel edge and ends at station 36, near the outer dish rim. The curve with the station-indicator marks is one actual interferometer record, while the nearby, somewhat heavier, curve is the average of the above with another record taken with the slave-cart wheels reversed 180° (see text). The smooth curve is the best-fit paraboloid $y = A + Br^2$ to the data. The corresponding deviation of the cat's-eye retroreflector apex from the true focus is indicated on the chart (ξ, η). The rms deviation of the observed curve from the best-fit paraboloid for this case was 3.7 μm .

The chart record is first analysed for the effects of incorrect placement of the retroreflector R by least-squares fitting. Thus the radial and vertical placements ξ and η of R are evaluated and may be corrected by moving R. The residuals are then treated as the errors to be removed by track adjustment.

Sagmeter data are needed because the interferometer errors do not directly represent local track errors, but rather a running average of errors of points displaced one station away from the mirror M in each direction. If h_i is the track height (perpendicular to the track) at station i , the interferometer residual at station i measures

$$I_i = \frac{1}{2} (h_{i-1} + h_{i+1}) \cos \theta_i$$

where θ_i is the slope angle of the track at station i . On the other hand, a sagmeter having the same two-station spacing as the cutter cart measures

$$S_i = h_i - \frac{1}{2} (h_{i-1} + h_{i+1})$$

Thus

$$h_i = I_i / \cos \theta_i + S_i.$$

(If the lateral track tilt B_i is not zero, an appropriate term $0.4 B_i$ must also be included, with appropriate sign, because of the lateral offset of the cutter blade from the track.)

A typical sagmeter record is shown in Fig. 12.

Figure 12: Reduced-scale sagmeter record for cutter track. The chart record starts at the lower left and proceeds (increasing radius) to the upper right. To accommodate the full signal range, a scale zero-offset was made, and the track partly retraced, between stations 25 and 30. The least-squares best-fit to the theoretical curve for the desired parabola is shown. The fine sawtooth structure is due to the cog-and-rack drive system and indicates that the noise level of the transducer is less than the chart line width. The sudden jump near station 15.5 is due to a step in the track at that point.

4. Retroreflector.

Because of the small focal ratio of the dish, the laser beam arrives at the retroreflector over almost a 60° range of angles. The glass retroreflector is unable to accommodate such a range and must be progressively realigned by rotating about a horizontal axis to maintain beam lock and to avoid introducing spurious path length errors. The effective optical apex of the glass corner-cube reflector is accurately located to coincide with the mechanical rotation axis and the assembly is rotated in approximately 10° steps by remote push button control. The effective focal point of the system, then, must be made to coincide with this rotation axis.

By repeated use of the above procedures, the cutter track was adjusted to within $7 \mu\text{m}$ rms for DISH 1 and $3.7 \mu\text{m}$ rms prior to machining DISH 2. The ultimate target accuracy for this term is $2 \mu\text{m}$ rms for the special i.r. dish.

5. Long-term stability.

It is of course essential that the cutter track retain its adjustment over a sufficiently long period to permit final cutting of the honeycomb without loss of accuracy. Diurnal thermal changes are not serious in this respect, inasmuch as the high-bay shop in which the dishes are fabricated is the cork-lined optical shop in which the 5 m Hale telescope mirror was ground and polished. By comparing two interferometer records taken eight months apart without having overtly disturbed the template girder, the rms point-by-point difference (after removing the effects of retroreflector shifts) was found to be $2.2 \mu\text{m}$. Note that this includes not only possible cutter track changes per se, but also upper track changes, any inconsistencies in the way the cutter cart rides on the track, and any inconsistencies in identifying "corresponding points" on the two records. Further, being the difference of two independent measures, the actual stability is probably better than $1.6 \mu\text{m}$ rms. Thus if the adjustment goal of $2 \mu\text{m}$ rms can be reached it should be possible to use such accuracy practically.

6. Air bearing; water manometer ; alignment telescope

The air bearing consists of two similar toroids of rectangular cross-

section. The approximate dimensions are shown in Fig. 9. The mating surfaces are ground flat. Air at a pressure of about 1 atm is admitted to the lower ring and the air escapes through some 200 adjustable nozzles into the space between the mating surfaces. About 0.3 atm pressure is sufficient to "float" the upper ring and dish. As operated, the air gap is about 100 μm thick.

The dish is supported symmetrically at three points on the upper ring and the dish structure is carefully centered with respect to the bearing ring. The lower bearing ring is partially supported symmetrically at three points on rigid 10:1 lever systems having fine-threaded screws at the extreme ends of the levers. This provides a means for leveling the bearing. (Fig. 9).

The weight of the dish and the stiffness of the air bearing structure are such that significant deformations of the bearing occur as the dish rotates. In addition, small but measurable distortions in the unloaded rings exist, which also cause significant effects. The principal such effects are 1) a possible 3rd harmonic (3 cycles/revolution) vertical translation having maxima where the dish support points pass over the lower ring support points and minima at the intermediate positions, and 2) a wobble of the rotation axis as the 2nd harmonic "saddle" distortions of the rings interact with the 3rd harmonic elastic sag of the rings.

The latter effect is easily observed in a sensitive water-manometer leveling system that is built into the dish structure. Attached to the dish frame near its outer edge are three equally spaced rigid platforms. Two of these carry Erlenmeyer flasks and the third carries a glass manometer riser tube having a 5 mm bore, and a 50X viewing microscope. Radial tubes connect these platforms to a circular ring tube near the dish axis. Hose clamps at the two flasks permit one or the other to be closed off, so that one flask and the riser tube will act as a leveling manometer between the two corresponding platforms. (The radial tubes and circular ring reduce sensitivity to angular acceleration effects. The tubing size is selected to provide critical damping for ordinary water as a manometer fluid. Trisodium phosphate is used to give good wetting of the riser tube.) As the dish slowly rotates, manometer readings are recorded and also entered into an HP-67 calculator Fourier coefficient program. Twenty four such

readings yield consistent fundamental (tilt) and third-harmonic terms.

In principle (and in practice for the case of the prototype dish), the effects of such an axis wobble could be corrected by using the 99 panel-support adjustment screws. However, it is preferable to eliminate the error directly if possible. The following remedial actions effectively removed the problem for DISH 1:

Nine intermediate supports (carriage bolts threaded into the bottom ring with their heads pushing down on segments of heavy automobile leaf spring) were introduced to help distribute the floor-support forces on the bottom air bearing ring. The leaf springs provided sufficient compliance to permit leveling adjustments to be made without having to re-adjust the carriage bolts.

A lever-and-weight system was attached to the top bearing ring so as to remove some of the dish weight at the three support points, transferring it to intermediate points of the top ring.

An I-beam complex was attached to the top ring so as to counteract the effects of the built-in saddle-shape of that ring.

None of the auxiliary beams or levers touches the dish structure itself: The dish is symmetrically supported at only three points.

The dish rotation axis is rendered accurately vertical by the manometer measurements and air bearing tilt adjustments just described. The rotation axis is then made to pass through the cutter-track focus F by lateral adjustment of the top air bearing ring. (The ring position is defined laterally by four adjustable cam-follower bearings equally spaced about its periphery (CF in Fig. 9). The alignment is measured using a telescope AT attached to the dish structure at a place where it looks through a feed-leg hole in the panels. The telescope is aimed at a small, aluminized sphere, SR, accurately centered with a vertical line through F. Near the telescope is a small flashlight bulb, whose virtual image in SR appears as a "star" to the observer, O. The lateral motion of this "star" against a reference reticle as the dish revolves measures the amplitude and phase of the axis misalignment. Correction of the misalignment is then straightforward.

7. Cutters and cutting.

Initially, the advice from knowledgeable people in the aircraft, aerospace, and honeycomb materials industries was discouraging: aluminum honeycomb could not be machined satisfactorily without stabilizing it with frozen glycol or other similar means. However, the special circumstances of our planned application seemed sufficiently favorable that it was resolved to try it anyway. The few successful cases we learned about seemed to involve the use of fine-toothed, high speed, thin, saw-like cutters. Commercial saw blade vendors agreed. Four kinds of cutters were used, and all worked reasonably well.

For removing the paper "skin" which is commonly attached to the open honeycomb as received, and for hogging away 2 cm or so of honeycomb from the centers of panels an ordinary 20 cm diameter, carbide-tipped table saw blade is used. This blade does tear the honeycomb cells to a depth of about 5 mm below the nominal cut level, but permits deep cuts and handles the paper and glue without trouble.

For finer cuts and the finish cuts, a flat-faced, hollow-ground, knife-edged, high-speed tool steel slicing blade, hard-chrome plated after sharpening, is preferred. Serrations (a la kitchen paring knives) also work well, as do small, beveled triangular teeth running "backward", i.e., slicing rather than chiseling.

The cutters operate at 3450 rpm, and are screwed to a heavy stabilizing flange on the end of the motor shaft. The cutter is as nearly as possible touching the honeycomb all around. (That is, the cutter motor axis nearly intersects the dish rotation axis at the local sagittal radius of curvature.) For practical reasons, a clearance of perhaps 50 μm at the trailing edge of the cutter is introduced. A cutter lasts for many cuts of the entire 85 m² surface and even a much-used cutter might yield a satisfactory finished surface. However, a new cutter is generally used for the last few light cuts.

Cuts as heavy as 1 mm are initially made, until the torn cells left by the saw-blade cutter are gone, and/or until perhaps 5-6 mm are left to go. (At this point the panels are all removed, cleaned, painted, etc., as described elsewhere, and replaced on the dish.) Finish cuts range from 500 μm to 50 μm , the latter being not so much cutting, as scraping, pounding, and grinding.

Three principal kinds of error are associated with the cutting operation: scalloping, crowning, and thermal distortion.

Scalloping arises from the fact that adjacent circumferential cuts are separated by a finite radial step. If the cutter axis were to precisely intersect the rotation axis, the shape of any one circular traverse would be a sphere of radius equal to the sagittal radius R_s of the local paraboloid. The meridional radius R_m differs from the sagittal radius, however, introducing a series of scallops whose radius of curvature relative to the parabolic curve is $1/R = 1/R_s - 1/R_m = (y/f)/2f(1+y/f)^{3/2}$. A radial step $2s$ gives rise to scallops of depth $\delta = s^2/2R$. Near the outer edge of the dish, this depth would be about 9 μm for $s = 2.5$ cm and would contribute about 2.5 μm to the rms surface error.

Crowning is the distortion of panel surface shape by the elastic forces of deformation of the panel top skin. The top skin, initially flat, is distorted into a bowl-shape by external pressure and then held in that shape by the honeycomb. Correspondingly, the honeycomb is distorted, becoming slightly convex relative to its original shape. The maximum amplitude of this effect was approximately 150 μm on uncompensated prototype dish panels, and was reduced several fold on DISH 1 panels through a combination of thicker middle-and lower-panel skins and systematic pre-straining of panels during the cutting operation. A simple T-shaped plywood truss, supported by three aluminum rods slung between eye-bolts attached to the panel corners, pushes upward at the panel center and pulls downward equally at all panel corners, causing the center of the panel to be cut more deeply than the corners (see Fig. 13). The top-skin deformation forces then pull the panel center back up to the proper level.

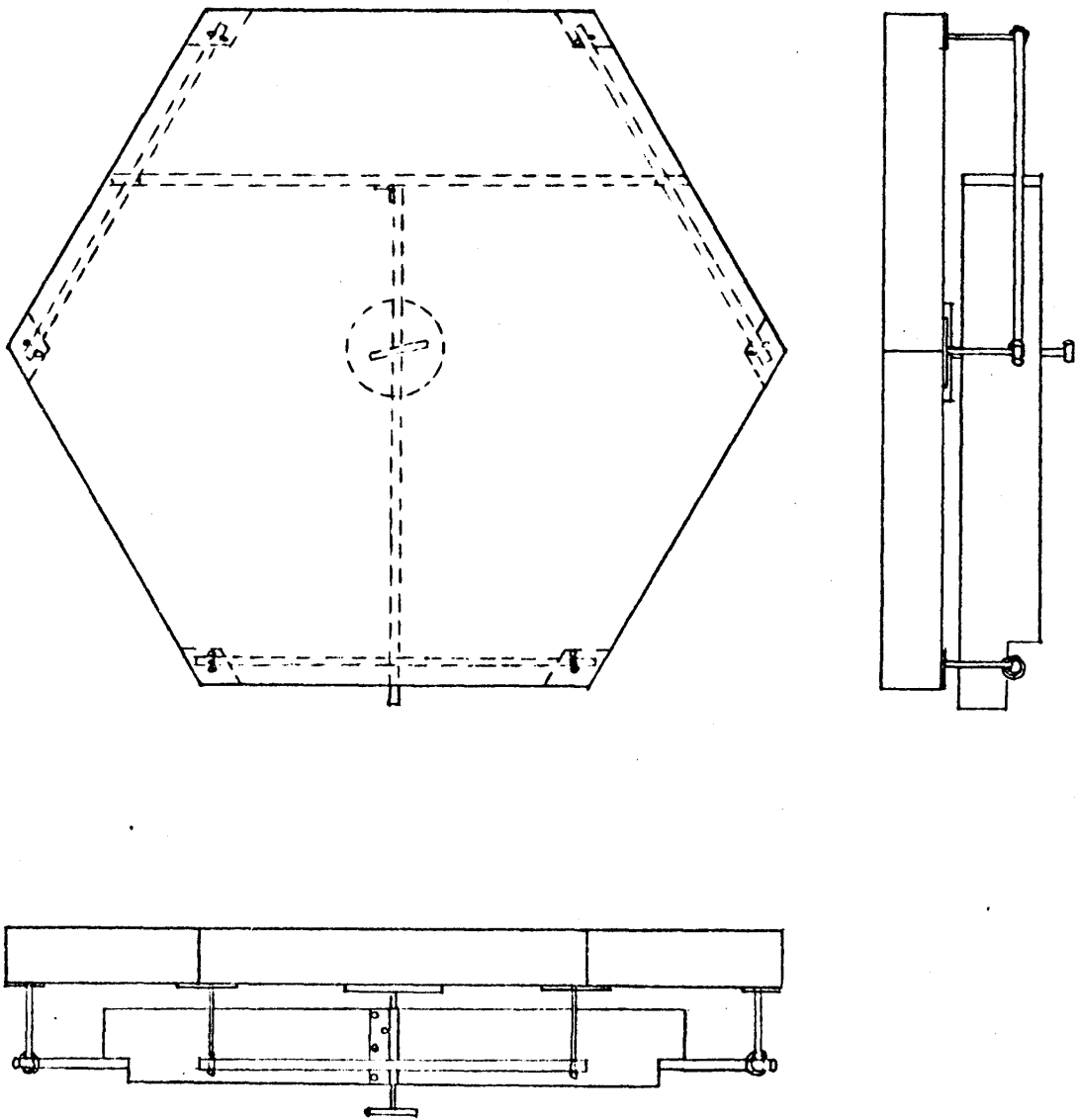


Figure 13: Schematic sketch of plywood panel "stretchers". Three aluminum rods are held by six eye-bolts attached to the panel corners. A hinged, "T"-shaped plywood frame rests with one arm at the center of each rod. A fine-threaded screw topped with a large circular "foot" presses upward at the panel center. The geometry of the support arrangement assures that equal downward forces exist at each corner.

Thermal distortion is caused by the temporary warping of a honeycomb panel by the heat generated by the cutting process itself. As the cutter advances, the frictional heat it generates is conducted downward through the aluminum honeycomb. As it reaches the center skin, that skin expands, rendering the panel locally convex. Depending upon the cutter location in relation to the panel supports, this may produce a raising or lowering of that part of the panel and of other parts about to be cut, causing these parts to be cut more or less deeply than desired. By the time the dish revolves once, bringing the given panel again into cutting position, the earlier heat pulse has penetrated to the bottom skin and the warping has disappeared. Thus a systematic effect, yielding a generally concave shape, results. This effect would be very difficult or impossible to calculate but can be minimized by using thick middle-and lower-skins, sharp cutters, and shallow cuts.

8. Panels.

Three further factors, in addition to those just described, affect the accuracy of the final panel surface: skin-to-honeycomb conformity, skin thickness uniformity, and the effects of removal-replacement of panels.

As cut, the exposed honeycomb cell edges appear smooth to the naked eye. Under magnification, however, they are seen to be jagged and ragged along one edge. During the ensuing cleaning and epoxy application via paint roller, one may worry that small chips may become broken off and lodged between the cut surface and the mating top skin. If this occurs at all, it does so rarely. More prevalent are cases in which a shred of cut material fails to be removed during the compressed-air cleaning stage and becomes caught astraddle a cell edge. Such occurrences also are infrequent, probably less than one per panel. Such pimples and other irregularities, if noticeable at the time the skin is first applied, can be reduced by vigorous, systematic hand rubbing of the skin surface while the panel is on the vacuum table. Judicious tapping with a rubber mallet is also a possible remedy, since it takes but little force to drive the chip into the thin honeycomb cell material.

Thickness variations of the skin sheet stock are a small but significant error source. They are thought to amount to less than 6-7 μm rms, and might be reduced by even more careful selection of the skin stock. Inasmuch as this error is so much smaller than the other errors previously mentioned, it is possible that whatever post-fabrication techniques may be used to improve the larger scale panel shapes would also help to reduce the thickness errors. In particular, if lapping of the panel surfaces were to be done, this would presumably also remove the smaller-scale rolling marks as well.

9. Panel Measurement methods.

After the top skins are cemented to the honeycomb panel faces, the panels are re-mounted on the support frame and the mounting screws are tightened, using a torque wrench and following a definite pattern to assure reproducibility. The dish surface shape is then measured by an electronic linear transducer situated precisely where the cutter blade leading edge had been, the dish being rotated past the transducer just as during the final cutting operation. The resulting analog signal may be digitized and stored on magnetic tape, recorded on a strip-chart recorder, or transferred to the dish surface itself. The first two recording methods are straightforward. The third method, perhaps the most useful, will be described further.

The objective of the panel shape verification tests is to evaluate the surface shape of the dish with a view to understanding the nature and origins of any errors, to evaluate the surface rms error, and to obtain the necessary data to optimize the dish shape by resetting the panel support differential screws. The third method leads to an actual, full-size contour map of the deviations of the panels from a paraboloidal shape.

The basic principle is to mark the dish at each local point, automatically, with a different color felt-tipped marker according to the local surface height. This is accomplished as follows. The transducer

signal is recorded on a strip-chart recorder on a sensitive scale of, say, 10 μ m surface height per cm of deflection. A series of equally-spaced, normally closed magnetic reed switches is mounted alongside the pen-travel guide, and a magnet is attached to the pen carrier so as to open the switches in a nearly - or slightly - overlapping sequence. Each switch is connected in series with one or more other switches displaced five units in either direction along the sequence. Thus switches 1, 6, 11, ... form one series circuit, switches 3, 7, 12, ... form another, etc.

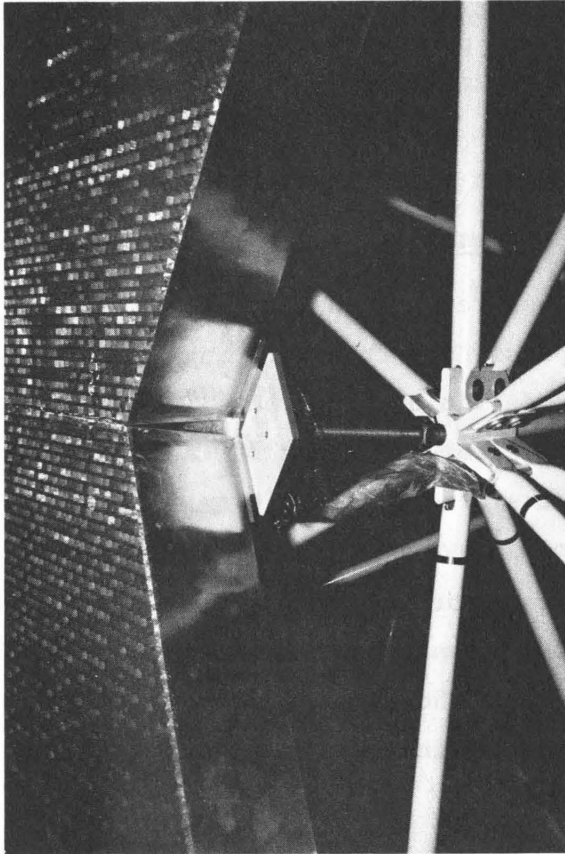
Corresponding to the five series of switches, five differently colored felt pens (red, orange, green, blue, purple) are held suspended a few millimeters above the dish surface by five solenoids, and a pen is released whenever one of its series-connected switches is opened. The pen marks the dish surface at a point within a few centimeters of the transducer, and continues to mark the dish until its circuit is again closed, and its solenoid energized. The resulting multicolored circular arcs, spaced about 7 cm radially, together with the chart record itself, provide sufficient data to draw an accurate contour map of the dish surface, on the dish panels themselves.

Figure 14: Four views of the prototype dish during construction. a) Close-up view of a panel support strut. Initially, each strut carries three (or sometimes two) so-called "diamond-plates". When a panel is to be attached to the dish, a dollop of epoxy is placed on each of the appropriate three diamond plates, and the panel is set in place. The diamond plates are henceforth a part of the panel. b) The honeycomb cutter saw in action. Note the thin slice of honeycomb being "peeled off" by the cutter. Visible in the picture are the cutter and the cutter motor, the depth-feed adjustment screw, vertical and lateral adjustment screws for one cutter-cart "foot", the cutter track, the template girder, and the wooden catwalk, supported independently of the template girder, which provides access to the girder, tracks, cutter cart, and dish surface. c) Overhead view of the roughing-cut stage of the prototype dish. The circular patterns represent the intersection of the paraboloidal cutter surface with the polyhedron made up of plane panel faces. The cutter is situated about midway from center to edge. d) The reassembled dish after the panel skins were attached.

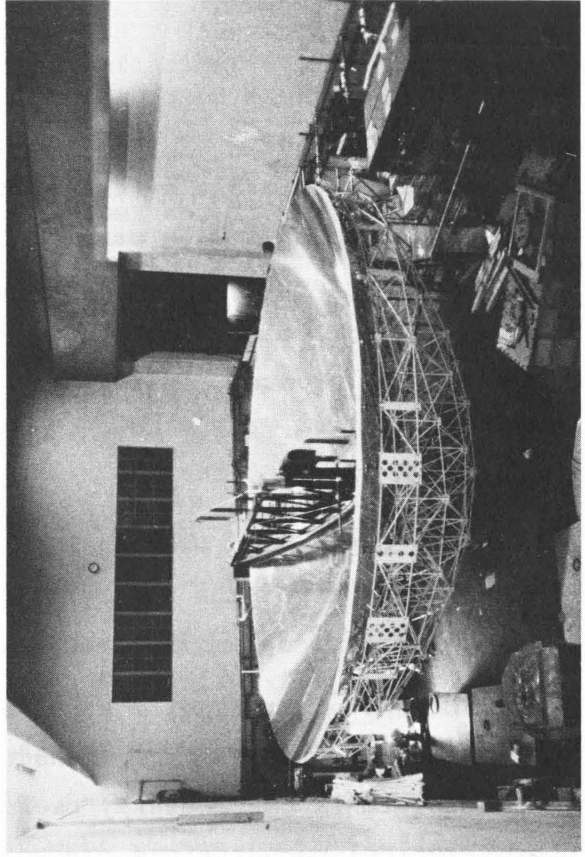
b



a



d



c

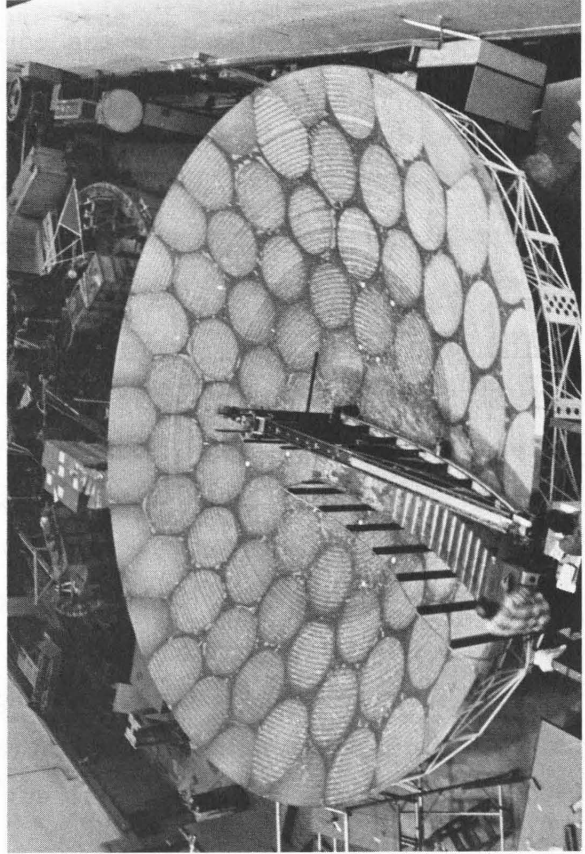


Figure 14

Looking ahead to the third dish of the series, a special effort will be made to improve the surface shape and smoothness of that dish beyond the values attainable by the procedures described up till now. For example, the contour map of each panel will be used as a basis for preparing a sequence of sheet plastic etching masks, and the various high areas of a panel will be selectively and quantitatively etched away by dilute NaOH solution to produce, as it were, a flattened Fresnel lens-like version of the original surface. Further smoothing may be attained by lapping the resulting surface.

Photographs of the panel contours have been found useful for calculating moments of the contours with respect to the support points, for the purpose of optimally readjusting the panel differential screws.

On the other hand, most of the surface-shape maps in this report were prepared by computer from transducer data recorded on magnetic tape. The latter form is particularly useful where comparisons, differences or other arithmetical computations are to be made.

Errors introduced in the course of panel removal-replacement were measured on the prototype dish and were found to be less than about 10 μ m rms, as described in the next section.

10. Support-frame disassembly-reassembly. (DA/RA)

Early in the design period it was recognized that a dish of 10 meter diameter could be difficult and expensive to transport any great distance from its construction site to the observation site where it would be used. Inasmuch as the logical construction site - at least for a prototype version - was the Caltech campus, and the likely observatory site was Owens Valley Radio Observatory some 250 miles away, considerable attention was paid to the possibility of removing or greatly reducing the transport problems by making the dish easy to dismantle and reassemble. This in itself is not difficult to arrange, but the added requirement that dimensions be preserved to within a few micrometers throughout the process made the problem a more challenging one.

The adopted solution was simply a refinement of the principles and procedures used on the 3-meter dish referred to earlier: 1) a geometrically simple structure having a high degree of symmetry was used so that many members would have identical lengths, 2) the dimensional tolerance problem was reduced to its simplest terms, i.e., to the control of linear distances alone, and 3) problems of warping and internal stress were avoided by using close-fitting pinned joints rather than welded joints.

Elastic tests on actual joint models established that the penalty incurred by the use of pinned joints was a minor decrease in stiffness, approximately 15-25 percent, as compared to ideally perfect joints.

Lengths were held to within $\pm 10 \mu\text{m}$ tolerances through the use of the same laser interferometer that was used to establish the cutter track shape.

All holes were initially made approximately $25 \mu\text{m}$ undersized. After the posts and struts were cleaned and painted, just prior to assembly of the support frame, the holes were brought to the desired $\pm 5 \mu\text{m}$ tolerance by hand reaming, using go/no-go gauge pins as a check.

The frame was assembled on the air bearing, whose rotatability greatly speeded the process. Each strut was initially held in place temporarily by a soft steel pin, about $25 \mu\text{m}$ undersized, which could be slipped into place by finger pressure. When a set of three struts connecting two adjacent posts had been so assembled, each temporary pin was carefully replaced by a full-sized alloy-steel tubular pin, using a soft steel tapered setting punch and a light hammer. Vise-grip pliers were used to prevent bending of the flattened ends of the strut.

Although in principle the support frame could be completely disassembled and reassembled, disassembly into three major pieces was sufficient for the purpose, and therefore, in order to maximize the stiffness, a one-component bakeable epoxy was introduced into all joints except those that were later to be disassembled, and the epoxy was cured using 300 - 400 W electric heaters attached to the "spiders" at the top and bottom of each post.*

*DISH 1 and subsequent dishes only. No such epoxy was used in the prototype dish

Certain special aids and procedures were devised to facilitate DA/RA and to avoid over-stressing any joints in the process. Nine wheeled jacks of different heights were built to support the three frame sections when they are apart from one another. These jacks are topped with heavy calibrated die springs and, when emplaced, are screw-adjusted to apply the appropriate support forces prior to disassembly. The three jacks supporting a given section are connected together by wooden struts to permit moving each section about with ease and safety.

To test the validity of the DA/RA concept, the prototype dish surface was measured and the measurements stored on magnetic tape. The panels were then removed, the support frame disassembled into its three parts, and the reverse procedures were used to reassemble the dish. A second set of measurements was made, and the two sets were compared point-by-point. The two sets were in good agreement except near the two ends of one of the chords along which the frame was parted, where local errors of as much as 200 μm were seen. Evidently some stress had been present which was partially relieved in the DA/RA process. *

As a further check a second DA/RA cycle was carried through and the surface was again measured. No further changes were observed. The second and third measurement sets were used to characterize the process. Henceforth, each dish frame is routinely cycled once, prior to final machining of the honeycomb panels. No recognizable signs of DA/RA strain were present in DISH 1.

The errors introduced by DA/RA were estimated by comparing statistically the point-by-point differences between the second and third measurement sets with two similar measurement sets made on the same surface on successive days. The rms fluctuations of the former were 21 μm , and of the latter, 20 μm . The rms difference of these is 6 μm which, while not to be taken too seriously, does suggest that errors comparable to the measurement errors of approximately 15 μm were not introduced in the second DA/RA cycle. subsequent experience with DISH 1 is also in agreement with that conclusion. The above-described effects are illustrated in Figs. 15 - 19. Fig. 20 shows further aspects of dish construction.

*During the assembly of the support frame for DISH 1 a dimensional error in a certain outer-rim spider fin was found which could have caused such stress, and in fact the outer rim of the prototype dish was difficult to assemble, probably for that reason.

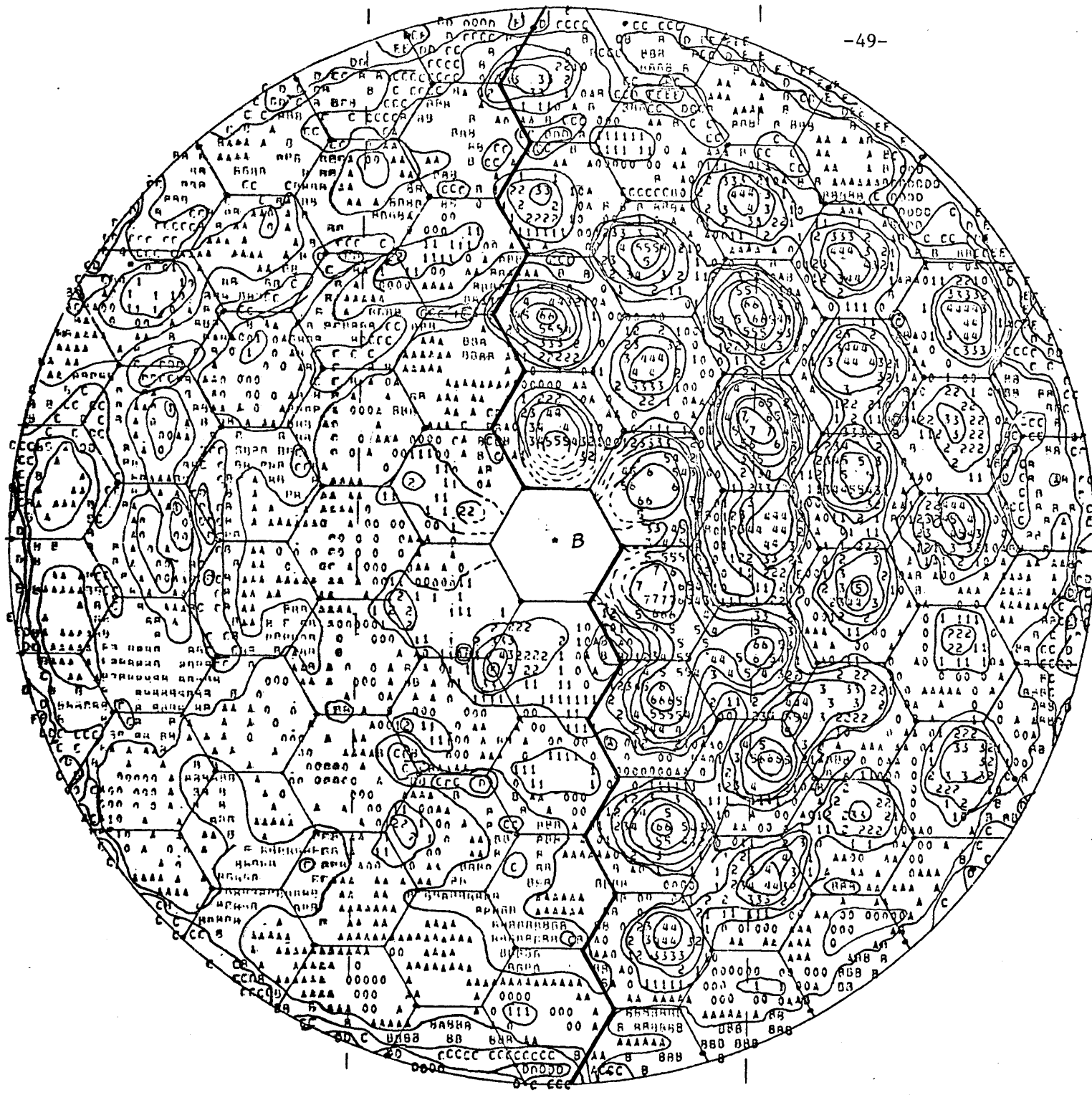


Figure 15: Computer map of prototype dish surface as measured following the initial remounting of the panels. Approximate boundaries of the panels are drawn in, and approximate, hand-drawn contours are shown. Positive heights above a best-fit paraboloid are indicated by the digits 0-9, negative heights by the letters A-I, in 25 μm (0.001 inch) steps. If a given point does not fall within $\pm 1/4$ unit of an integer value, a blank is printed. The panels to the left of the heavy jagged line had "stretchers" attached and those to the right did not (see text). Note the obvious "crowning" of the unstretched panels as compared with the stretched ones. The rms surface errors for the two areas are 30 μm and 60 μm respectively, and the mean value is 50 μm .

TAUS TAPET

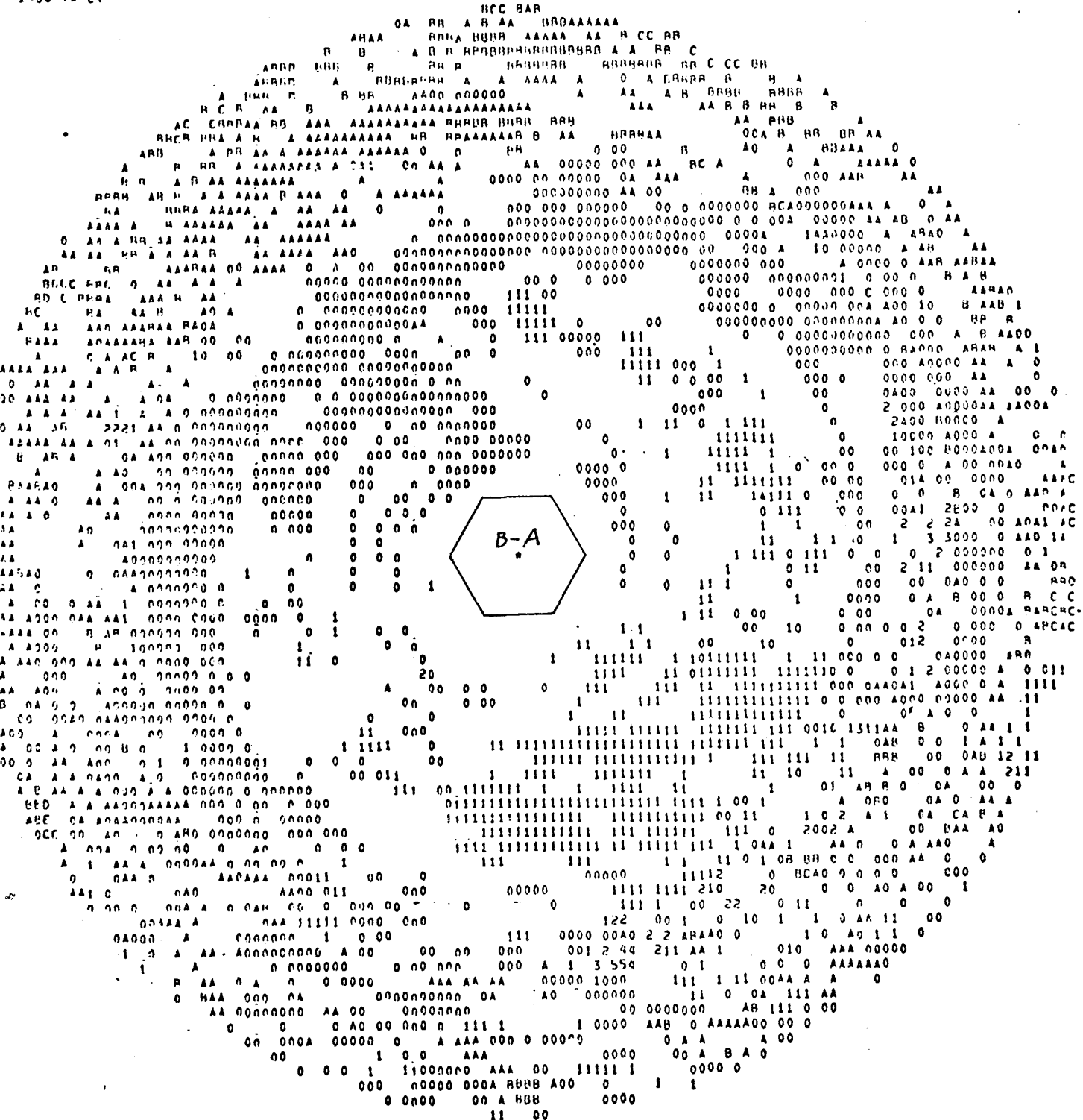


Figure 16: This figure is a plot of the point-by-point difference (1° in azimuth, 7.5 cm radially) between two successive measurements of the prototype dish surface. One of the data sets is that of Fig. 15. The rms difference is 20 μ m, which establishes the noise level of a single measurement as about 15 μ m.

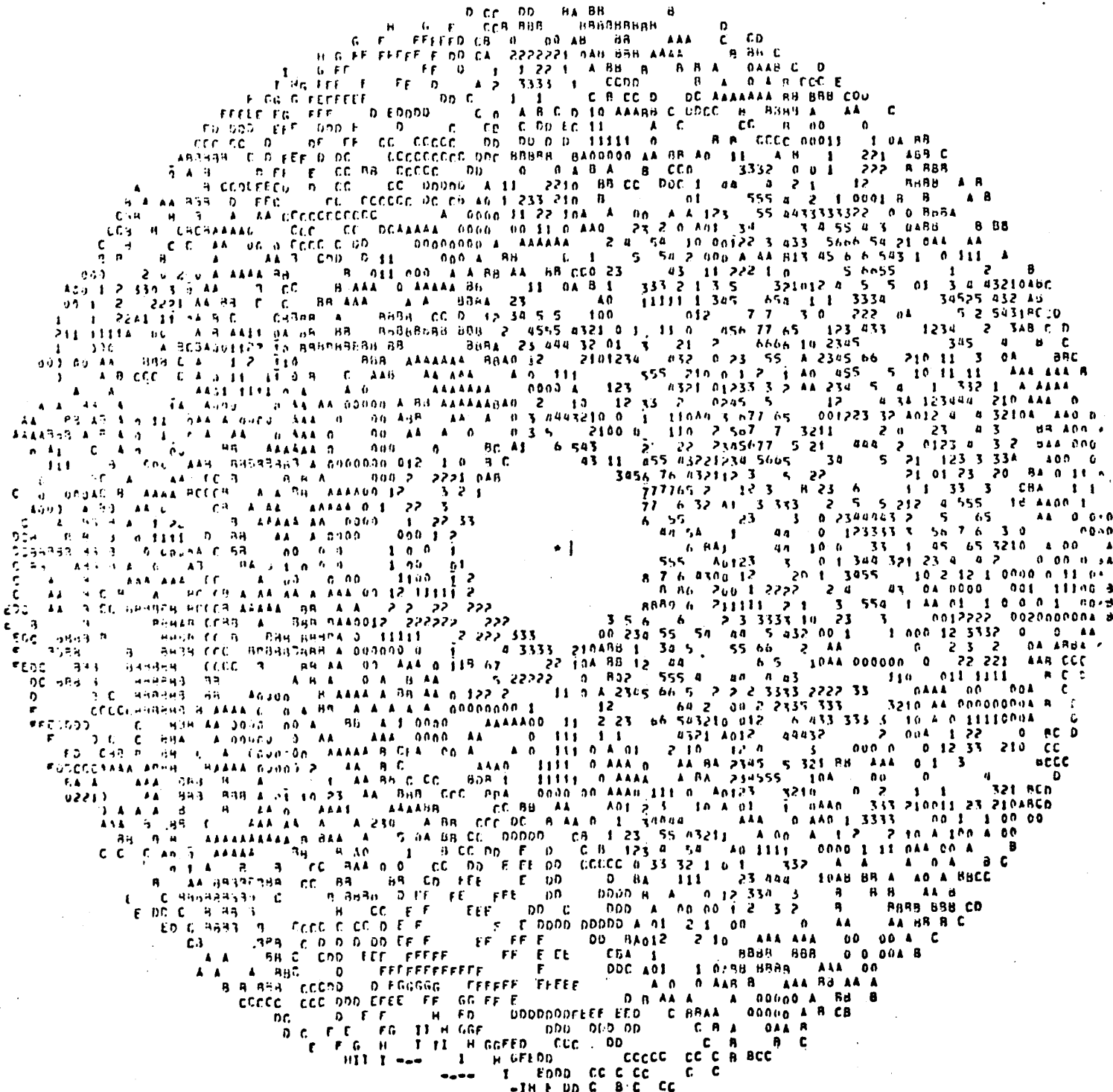


Figure 17: Prototype dish surface error map following first support-frame disassembly reassembly. Note the large, negative errors at the top and bottom, somewhat left of center. See Fig. 18.

MINUS TAPE 1

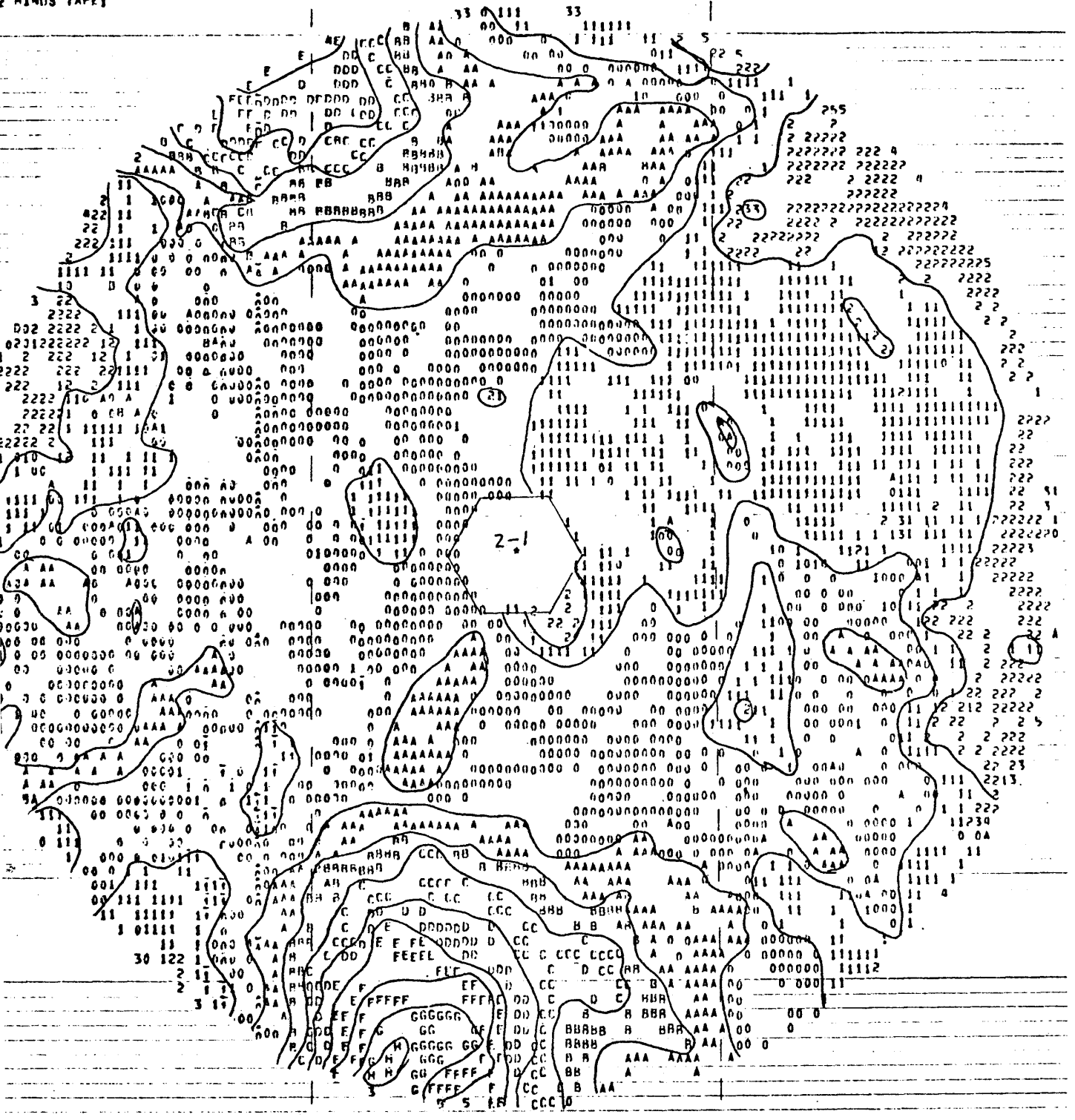


Figure 18: Prototype dish surface difference map, before vs. after disassembly/reassembly. The two low areas mentioned above are clearly seen. Contours are hand-drawn.

Figure 19: Difference map for 2nd DA/RA vs. 1st DA/RA. Here, the strongly affected areas have disappeared, i.e., there was no further change between the two DA/RA cycles. The effects were removed from the dish by readjustment of the panel-support differential screws. No similar problem was encountered with DISH 1, the first "production" dish.

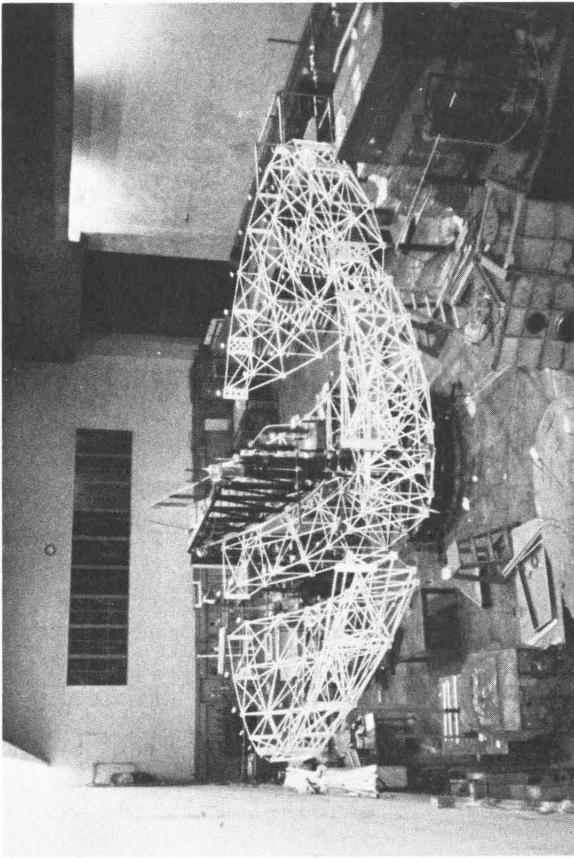


555 22

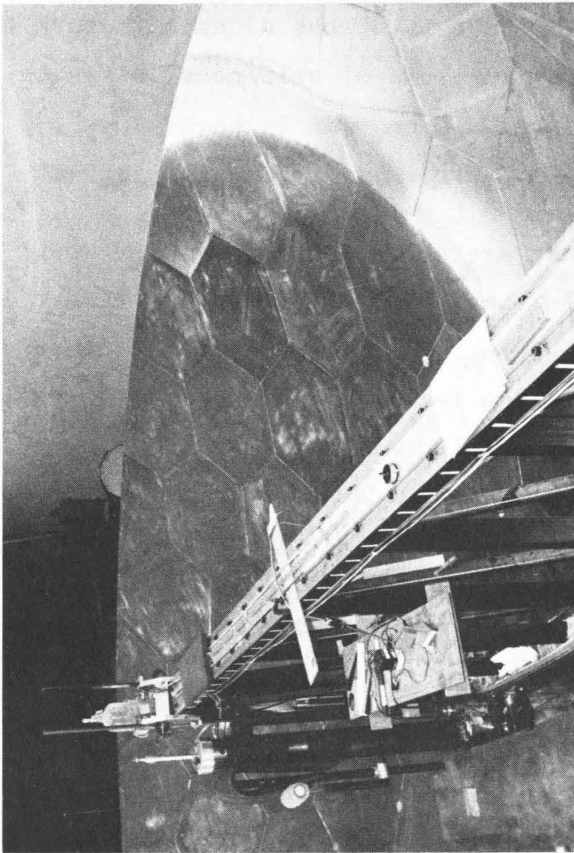
4002 47103 4461

Figure 20: Additional views of dish construction. a) Close-up view of finished prototype dish surface. Notice the curved "shadow-edge" crossing several panels at right. The serrated appearance of the outer part of this image is caused by the "scalloping" described in the text. The peak-to-peak amplitude of the scallops is approximately 25 μm . Also note the smoothness of the transition from panel to panel. b) View of the support frame during the first DA/RA cycle. The panels have been removed and the support frame parted into three parts by removing pinned struts. c) The central frame section being trucked to Owens Valley Radio Observatory. d) The reassembled support frame at OVRO. The dish panels are stored and shipped in the multi-layered "pie-racks", and are here ready to be reattached to the dish.

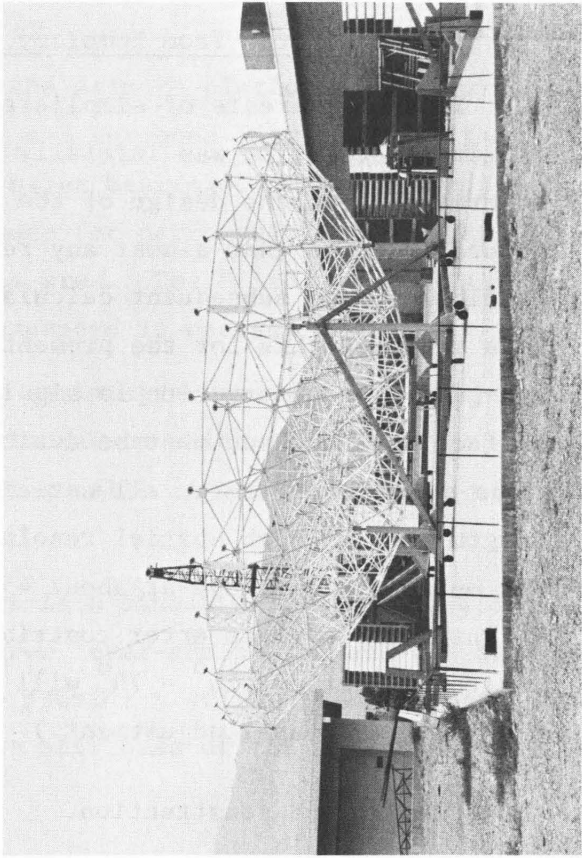
b



a



d



c

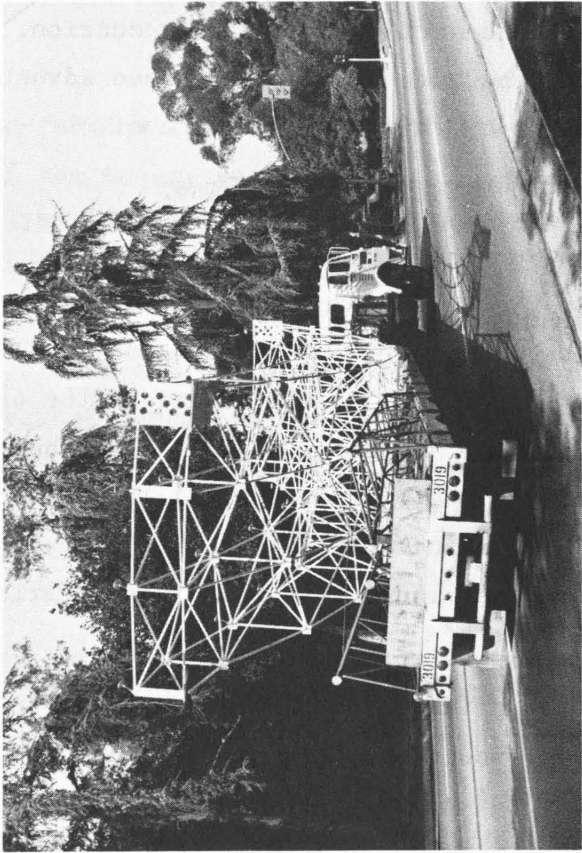


Figure 20

11. Departures from homology. Optimum panel adjustment.

In the interests of simplicity of design and ease of construction, no formal attention was initially given to the question of non-homologous deformations in the design of the 10.4-meter dish structure. It is generally found that almost any reasonably homogeneous structure is nearly homologous, and subsequent calculations of deflections at 90° zenith angle have verified this for the present dish. Nevertheless, the small remaining non-parabolic deformation is significant in comparison with the desired surface accuracy and must be dealt with. For wavelengths greater than about 1 mm, that is for all anticipated uses except submillimeter wavelength work at high spatial resolution, it suffices to readjust the panels for optimum dish shape at about 45° zenith angle. If this is done, the weighted rms surface error contributed by deviations from homology in the zenith angle range $10^{\circ} - 70^{\circ}$ will be about 6 μm . (See pp. 63,64 for further discussion of panel adjustment.)

II. Mount design and construction.

As described in the introduction, the mount is of the altazimuth fork type, chosen because of its recognized advantages in terms of stiffness, strength, movability, simplicity, and cost.

A. General description.

Schematic sectional views of the mount are shown in Fig. 4. The mount base is a square frame of heavy, wide-flange I-beams, with cross-members connecting opposite corners, and surmounted by a truncated steel-plate cone of octagonal cross-section. At the center of the base is a raised platform about 45 cm high, with a conical radial-thrust bearing mounted at its center. This bearing supports the entire vertical load of the movable telescope structure. At the top of the octagonal cone is a heavy steel ring, with eight radial thrust bearing assemblies mounted on it. These bearings will be described later.

The azimuth axis is an inverted circular cone, the apex supported by the lower radial-thrust bearing and the upper end, provided with a flame-hardened and ground ring, is constrained radially by the eight roller thrust assemblies mentioned above.

Bolted to the top of this cone is the azimuth platform. This weldment mates with and is supported by the cone and hardened ring, and is itself the support for the two elevation crossed-roller bearings. The azimuth platform provides a certain amount of working space for personnel, and mounting space for equipment, near the cassegrain focus area. The "floor space" is somewhat expandable, and could be considerably expanded if necessary.

The two vertical fork "prongs" are an integral part of the azimuth platform. They are capped by accurately machined ledges on which the elevation bearing housings rest and to the upward projecting walls of which these are securely bolted.

Supported by the elevation bearings is a single weldment comprising the elevation axis torque tube, the ball-screw lever-arm plate, and the dish-mounting platform. This unit is designed to provide a stiff, stable mounting base for the dish, one which will enhance the stiffness of the dish frame itself.

B. Special features.

Certain special features of the mount are worthy of note.

1. Bolt-on dish attachment.

Because of the particular dish-fabrication techniques that were used, the dish is not an integral part of the mount, as is often the case, but is bolted to it. This has the possible disadvantages that the dish-mount interface might detract from the overall stiffness and, moreover, might introduce unwanted distortions in the dish. On the other hand, the method affords easy interchangeability of dishes and convenient portability of dish and mount. In practice it does not appear to have significant drawbacks.

The dish-mounting platform is provided with 12 machined bosses and accurately drilled bolt-holes, having the same basic triangular pattern as the dish posts.

The dish is placed on the mount with the mount pointed toward the zenith; it rests on 1 cm-thick steel shims placed on the appropriate three bosses, so that the dish is supported at the same three posts as during machining. These three bolts are loosely inserted; adjustable (slotted,

tapered) shims are placed on the outer six of the remaining bosses and the corresponding bolts also inserted.

The first three bolts are then securely tightened, and at each remaining post the tapered shim is adjusted and its bolt secured, using a pair of sensitive dial indicators to assure that this is done without introducing significant strain. (Fig. 21).

2. Ball-screw elevation drive.

In the original mount design, pre-loaded anti-backlash gear drives were to be used in both coordinates. The high cost of large sector gears led to a reassessment of the elevation drive design, and it soon became apparent that a single, pre-loaded ball-screw actuator might provide a sufficiently stiff and accurate elevation drive at a fraction of the cost of an all-gear system. This was tried on the prototype mount and proved to be quite satisfactory in all respects save one: a 4-thread, 20:1 worm-and-gear speed reducer, used to match the ball screw pitch and lever arm to the drive motor slew speed, proved to have too much friction and moreover was subject to binding. An additional 2:1 reduction by spur-gears solved the problem at the expense of reduced slew rate. This problem is to be avoided in the subsequent mounts by using an all-spur-gear speed reducer at nearly the original 20:1 ratio.

Other than the friction problem just described, the ball-screw actuator elevation drive has proved entirely satisfactory. In particular, its variable lever arm is sufficiently well-modeled by a simple quadratic function of zenith angle as to present no difficulties in the servo control loop; the pre-loaded ball-nut cancels out backlash to within approximately 1/4 motor turn - a fraction of an arc minute - so that a second screw, gear train, and motor is unnecessary.

3. Epicyclic azimuth drive.

In azimuth, a commercial high quality, alloy-steel gear is bolted to the azimuth cone and is driven by two identical speed-reductor-and-motor

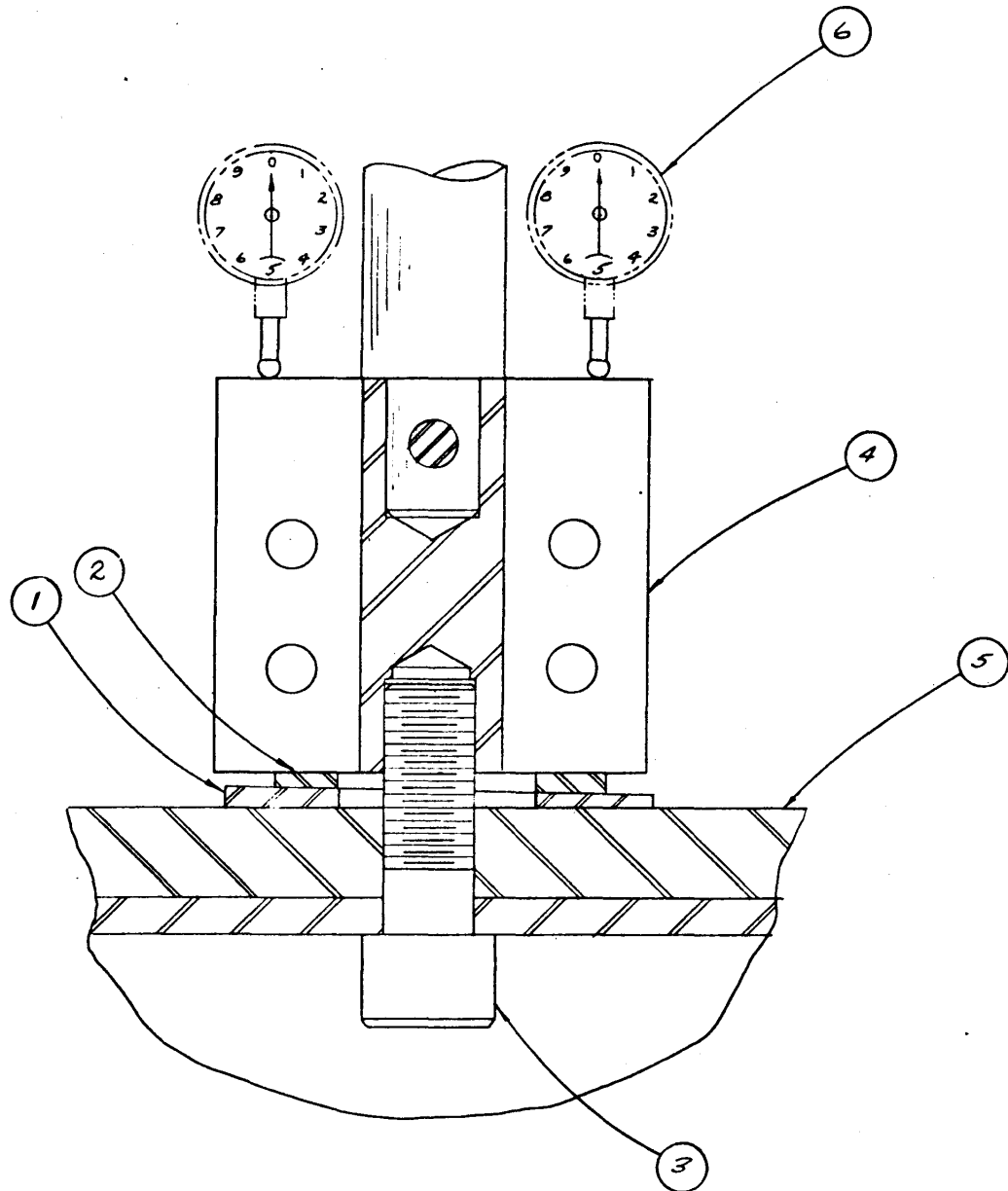


Figure 21: Schematic sketch of the bolt-down arrangement for six of the nine dish attachment points. Key: 1 & 2, tapered, slotted steel shims; 3, bolt; 4, spider and post; 5, machined boss-plate; 6, sensitive dial indicators, symmetrically mounted with respect to post axis.

drives in an anti-backlash mode described later. The 1505:1 speed reduction is accomplished by a two-stage epicyclic drive which operates on a principle similar to that of a differential pulley. These speed reducers are considerably less expensive and more compact than spur-gear reducers of similar torque rating and yet they have a similar high efficiency as compared to worm gear units (non-reversible worm gears would be inadmissible in this application because of the possibility of frictional lock-up). A possible disadvantage of the epicyclic drive is its somewhat greater backlash, but this can be minimized by special selection of certain components at the time of assembly (at a small extra cost) and in any case it has not been a limiting factor in tracking performance. (See the Servo section.)

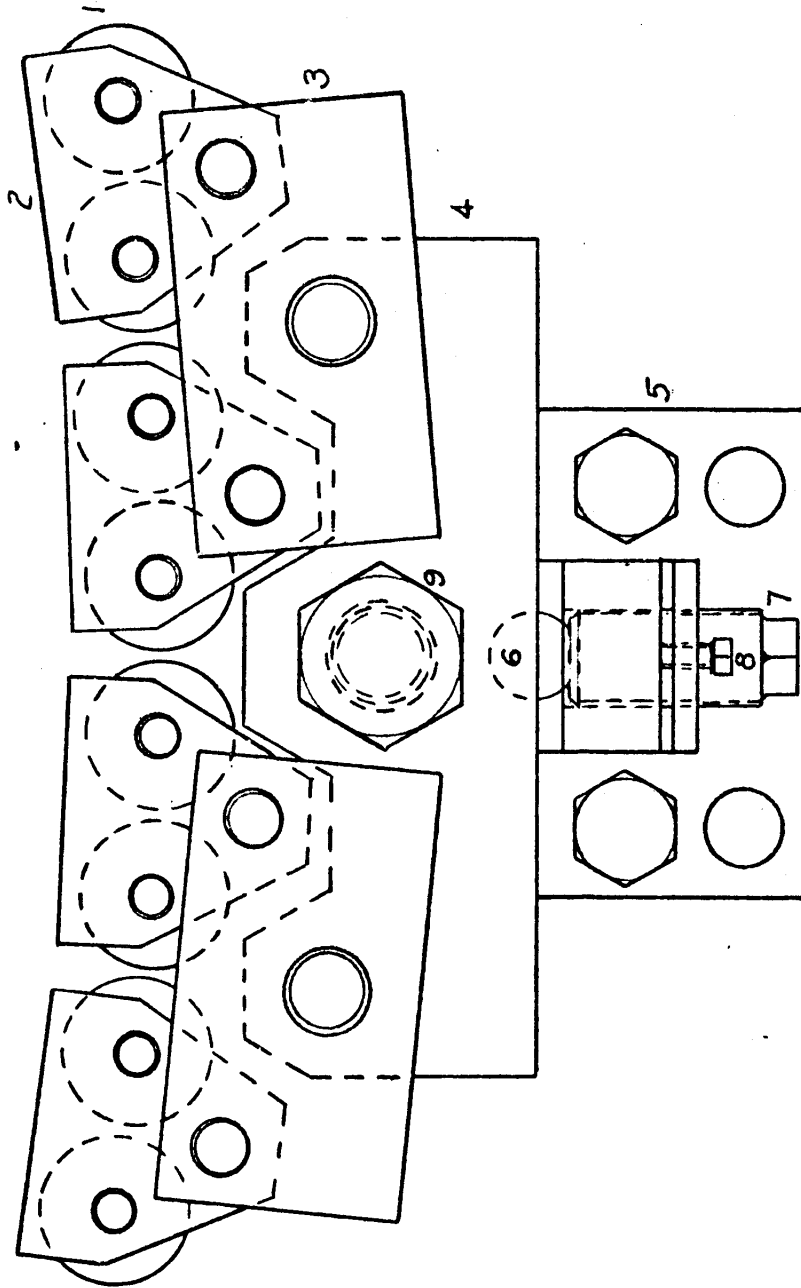
4. Roller-thrust assemblies.

The usual approach to the problem of providing a suitable upper azimuth bearing for a mount of the present type would be to use a large crossed-roller ring bearing at a cost of several thousand dollars. In the present application, where only radial loads are involved, a simpler and much less costly solution suggested itself: A narrow (1-inch wide), ground cylindrical ring is provided at the top of the azimuth cone, against which a number of stationary cam-follower needle-roller bearings roll. Sixty four such rollers, in eight units of eight rollers each, are equally positioned in azimuth about the hardened ring. Each unit is composed of a three-stage load-sharing arrangement similar to railroad-car trucks (without springs), whose radial position is defined by a rigid ball-and-socket screw adjustment system. (Fig. 22).

With proper adjustment (which involved in situ measurement of the effective force-constant of the roller units and the detailed out-of-roundness of the ring) the angular run-out of the azimuth axis was held to about one arc second.

Figure 22: Roller-thrust assembly. Key: 1, cam-follower needle roller; 2, primary pivot-plates; 3, secondary pivot plates; 4, tertiary pivot plate; 5, fixed base plate; 6, ball-and-socket; 7, thrust screw; 8, locking screw; 9, retaining bolt in slotted hole. Note: The ball is ground flat where it mates with the thrust screw 7.

Figure 22



8-ROLLER THRUST ASSY

5. Kinematic positioning

The intended interferometric use of the 10-meter telescopes and the short operating wavelength introduce certain design problems: 1) The telescopes must be easily movable between well-defined, fixed points. 2) The long integration times needed for faint sources requires that the baseline between any pair of telescopes be accurately known: The phase error during an integration interval must be much less than one radian. 3) There are very few bright "point" sources at millimeter wavelengths with which to calibrate baselines.

Thus, considerable care is needed to assure that the telescope will relocate reproducibly, on a given base pad, to within a few tens of micrometers, so as to minimize the time needed for baseline calibration.

At each corner of the square telescope base is attached an inverted (base-up) precision ball-bearing screw jack, with a precision footpiece at its lower tip. One footpiece is a hemispherical cup which mates with a fixed ball at one corner of the concrete base pad. The diagonally opposite footpiece is a concave semi-cylinder which mates with a convex semi-cylinder on the base pad. (The cylinder axis intersects the ball opposite.) The remaining two footpieces are flat, and rest on flat mating surfaces.

The square, four-leg support was chosen in preference to a three-leg design on the basis of greater stability for given base width, and easier adaptability to movement along E-W and N-S tracks. The minor disadvantage of static indeterminacy is overcome by a simple procedure which establishes the load at one corner to be one-fourth of the total weight: by moments, all four loads are then equal.

III. Adjustments and tests.

A. Axes: orthogonality and coincidence.

In the mount design, provision was made for precision longitudinal and lateral adjustment of the elevation axis bearing blocks and, by the use of shims, vertical adjustment as well. Thus it is possible a) to bring the azimuth and elevation axes into orthogonality within a few arc seconds, b) to assure that these axes intersect within a few tens of μm , and c) to bring the dish

vertex within a few tens of μm of the longitudinal plane containing the azimuth axis. These adjustments were made during the course of reassembly of the mount following the modifications described on p. 12, and can readily be rechecked as necessary. For ease of lateral adjustment, the bearing housings each rest on three heavy-duty crossed-roller thrust plates which permit free lateral motion of a few millimeters in any direction. (Fig. 4, item 14.)

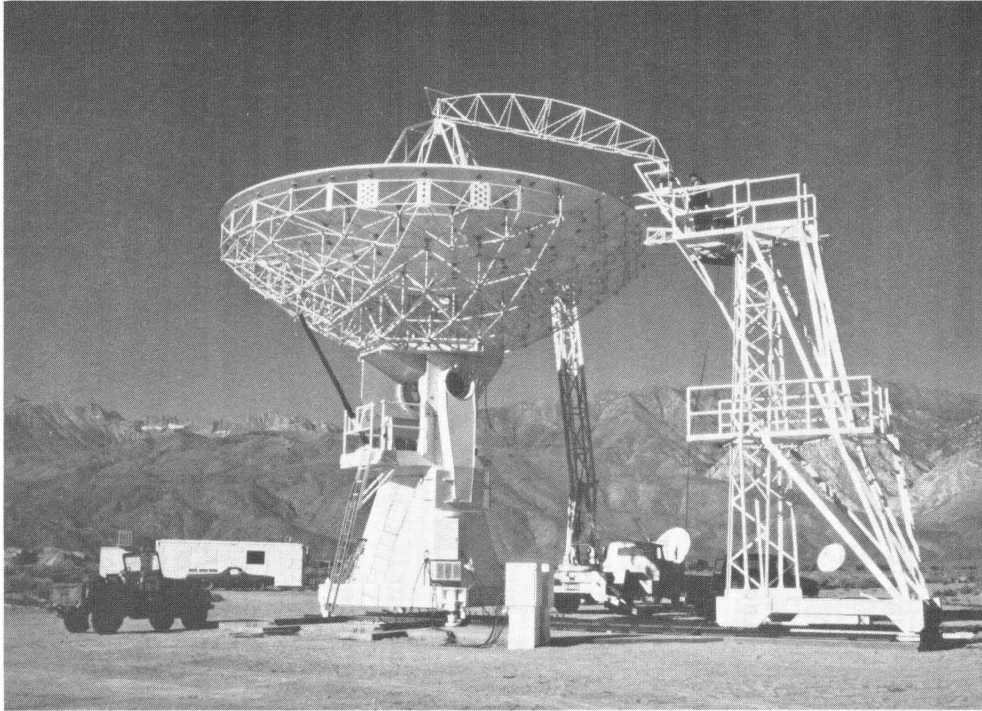
B. Dish panels

1. Measuring tower.

The panel-and-strut disassembly/reassembly procedures that were followed during manufacture and shipment of a dish were carefully devised to assure the preservation of surface accuracy through the final attachment of the dish to its mount. Nevertheless, over a period of time it is possible that unforeseen effects might alter the shape of the dish or of an individual panel; some method of in situ measurement of the dish and panel shapes should be available. For this reason as well as for its general utility, a stable, wheeled measuring tower was built adjacent to the prototype telescope (see Fig. 23). This tower has proven to be extremely useful not only for its original purpose of measuring the dish surface profile around the outer edge, but also for measuring the centering of the dish with respect to the azimuth axis, aligning the subreflector support, defining the zero-reference for the zenith-angle encoder, and providing ready access to the dish topside with the telescope in the zenith stow position. The tower is used during the assembly and adjustment of each telescope and will be available on a permanent basis to test and readjust the telescopes as necessary.

The first use of the measuring tower was to check the prototype dish surface profile around its outer edge by mounting a fixed transducer on the tower and rotating the dish past it. It was found that the dish surface near two support posts had become displaced by $100\ \mu\text{m}$ and $250\ \mu\text{m}$, apparently as a result of local disassembly/reassembly procedures that were used in placing the dish on its mount. (The available crane hoist could not lift the dish high enough without removing a few panels and support struts from the edge of the dish.)

A more elaborate check was made on DISH 1 (prior to the attachment of the feed-support legs) with the aid of a light,



(a)

Figure 23: Measuring tower and transducer girder. (a) West-looking view of telescope and measuring tower, with transducer girder in its position for aligning the sub-reflector support legs. (b) North-looking view of transducer-support girder, showing center bearing support and outrigger wheels. The top of the measurement tower projects above the dish edge.



rigid tubular girder supported at one end on the tower and at the other end on a ball bearing concentric with the dish vertex. A linear transducer, clamped to the curved lower stringer of the girder and touching the dish surface via a small cam-follower roller, could test the azimuthal height-uniformity of all panel support-points as well as the azimuthal panel profiles. In this way it was verified that the reassembled and mounted dish was of the same shape as measured in the laboratory, within the error of measurement (about 25 μm).

Thermal effects due to solar illumination and varying air currents introduce significant noise, but careful choice of measurement conditions, and repetitive measurements, permit useful accuracy to be achieved. Further improvements, such as the use of foam insulation on the girder, are planned.

2. Adjustment to optimum shape.

As described earlier (p. 56), it is desirable for work at short wavelengths to adjust the panel support screws to give optimum dish shape at about 45° angle. Actually, there are four distinct kinds of surface errors that should be dealt with in this adjustment:

- . effects of non-homologous deformation at elevations other than the zenith (p.56).
- . effects of air-bearing "wobble" (p. 37).
- . effects of disassembly/reassembly (p. 46).
- . effects of actual panel profiles (p. 44).

Of these, the first is calculable to sufficient accuracy by the dish deformation computer model (p. 20). The second is known from air-bearing manometer-level data and linear transducer azimuth profile records taken in the laboratory with the transducer near the dish center and near the dish edge, the transducer being situated at an appropriate angular displacement (60° or 90°) from the cutter track. This effect can also be measured after the dish is attached to the mount, provided the azimuth axis wobble of the mount is independently known, as it is for the present case.

The last effect arises from the fact that the various panels may

possess different amounts of convexity or concavity with respect to the nominal paraboloidal surface. Even if there were no errors in the panel heights at the 99 support points, these panel deformations would result in a non-zero surface variance. It then follows that the surface variance might be reduced by a suitable readjustment of the support posts. The actual panel height profiles, in the form of a contour map of the entire dish relative to the cutter-track curve shape as a zero-reference, are available. The least-squares problem of minimizing the residual variance is solvable to sufficient accuracy by iteration because each adjustment point affects at most three panels.

The prototype dish was corrected for the first three effects and a marked improvement in beam sharpness was noted. At an appropriate time, DISH 1 will be corrected for all four effects, but the uncorrected performance of this dish is already so good that only a small additional improvement is to be expected.

A computer printout of an approximation to the first effect for DISH 1 is shown in Fig. 24. The figure below shows two contoured panels, as described in the text (pp. 44, 46).



TOTAL RESIDUALS INCL FOURIER TERMS (0.1 MILS)

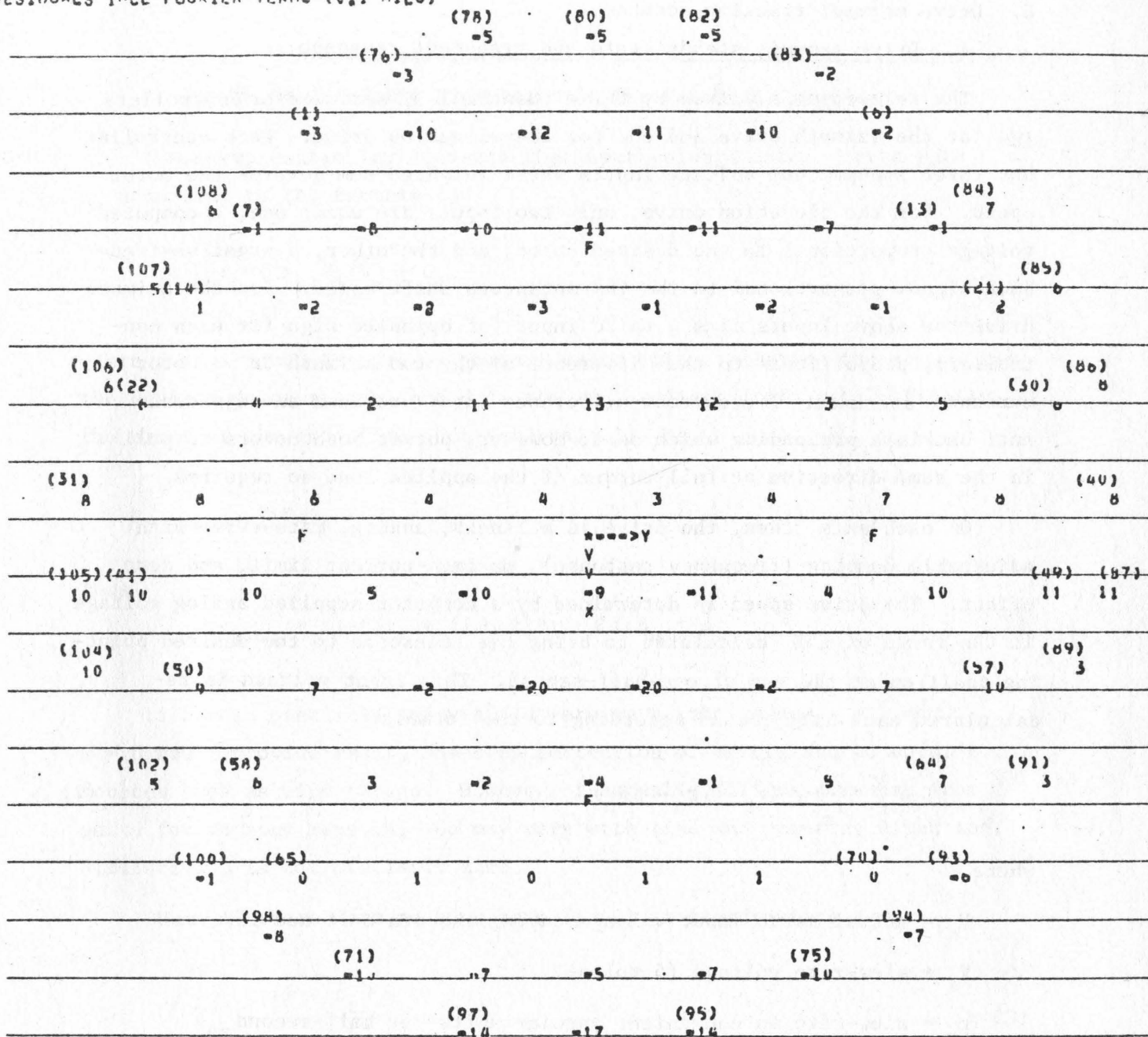


Figure 24: Computer map of the residual support-point heights relative to a best-fit paraboloid, at 45° zenith angle. The units are 2.5 μm (0.0001 inch). The actual adjustment of the support points will also include a component to account for the actual panel shapes (see text). The values shown are representative only. The actual values will differ somewhat to allow for the distortions due to the weight of the feed support structure which is incorrectly done in this figure. The rms deviation of the residuals as shown is approximately 20 μm. (Numbers in parentheses are post numbers.)

C. Drive servos; tracking accuracy.

1. Drive servos; steady state and transient response.

The telescope is driven by three identical DC servo-motor controllers, two for the azimuth drive and one for the elevation drive. Each controller has three independent voltage inputs whose weighted sum governs the motor speed. For the elevation drive, only two inputs are used: one, a computed voltage proportional to the desired speed, and the other, a negative-feedback signal proportional to the instantaneous shaft speed. For the azimuth drive the above inputs plus a third input (of opposite sign for each controller), proportional to the difference of the two azimuth drive motor currents, are used. The current-difference input provides an adjustable anti-backlash preloading which does, however, permit both motors to pull in the same direction at full torque if the applied load so requires.

On each axis, then, the drive is a linear, analog, rate-servo with adjustable damping (frequency response), maximum-current limit, and zero offset. The drive speed is determined by a computer-supplied analog voltage in the range of $\pm 5V$, calculated to bring the telescope to the desired pointing position at the end of one-half-second. This input voltage is recalculated each half second according to the formula

$$V_n = \frac{V_s}{r_s} (r_t - \gamma \epsilon_n - \beta B_n) \quad (1)$$

where

V_n = actual servo input voltage during the nth half-sec interval

V_s = slew-rate voltage (5 volts)

r_s = slew-rate in convenient angular units per half-second

r_t = desired tracking rate in same units as r_s

ϵ_n = pointing error at start of nth interval in same angular units as rates

$B_n = \sum_{i=-\infty}^{n-1} \epsilon_i =$ summed error to n-1 st interval (called the bias)

γ and β are dimensionless parameters which describe the magnitudes of the error-and bias-terms in the feedback loop.

The servo controller converts the input voltage into a drive rate r_n according to the formula

$$r_n = f r_s V_n / V_s + d$$

where f is a speed factor, of nominal value unity, relating the actual and the desired motor speeds, and d is the zero-voltage drift rate. Finally, the error at the end of the n th interval will be

$$\epsilon_{n+1} = \epsilon_n + r_n - r_t.$$

Thus

$$\epsilon_{n+1} = (1-f)r_t + (1-\gamma f)\epsilon_n - \beta f B_n + d \quad (2)$$

If f were precisely unity and d were zero, the values $\gamma = 1$ and $\beta = 0$ would provide exact, one-step correction of errors due to outside sources such as wind forces. However, f actually differs somewhat from unity for various reasons, and may vary with time and pointing direction. Similarly, d is not precisely zero.

Thus, if there were no bias term ($\beta = 0$), a steady-state error

$$\epsilon_{ss} = \frac{(1-f)r_t + d}{\gamma f} \quad (3)$$

would result. If the bias term is present, the steady-state error must become zero, and the integrated error is then

$$B_{ss} = \frac{(1-f)r_t + d}{\beta f} \quad (4)$$

The transient characteristics are most readily understood by a further modification of Eq. (2): Take the difference of (2) between two successive intervals to obtain

$$\epsilon_{n+2} - \epsilon_{n+1} = (1-f) \Delta r_t + (1-\gamma f)(\epsilon_{n+1} - \epsilon_n) - \beta f(B_{n+1} - B_n)$$

which simplifies to the second-order linear difference equation

$$\epsilon_{n+2} - (2-\gamma f)\epsilon_{n+1} + (1-\gamma f + \beta f)\epsilon_n = (1-f)\Delta r_t \quad (5)$$

where $\Delta r_t = r_{t, n+1} - r_{t, n}$ is the difference in the desired rates between the nth and n+1st intervals.

If Δr_t is zero (constant tracking rate), ϵ_n may be written

$$\epsilon_n = A \theta_1^n + B \theta_2^n \quad (6)$$

where θ_1 and θ_2 are the (real or complex) roots of

$$\theta^2 - (2-\gamma f)\theta + (1-\gamma f + \beta f) = 0 \quad (7)$$

$$\theta_{1,2} = 1 - \frac{1}{2} \gamma f \pm \frac{1}{2} \sqrt{\gamma^2 f^2 - 4 \beta f} \quad (7a)$$

A plot of the root values versus βf and $(\gamma - \beta)f$ is shown in Fig. 25. The roots outside the three heavy boundary lines lead to diverging solutions.

Figure 25: Plot of the characteristic roots (θ_1, θ_2) of the servo equation (7) as a function of the error - and bias - feedback coefficients γ and β , and the motor speed factor f . See text.

The stable region is divided into an oscillatory part (θ complex) and an exponential part (θ real) by the envelope parabola $\gamma^2 f^2 - 4 \beta f = 0$. The characteristic forms of the solutions in these regions are indicated in the figure. In general, solutions lying near an outer boundary decay slowly, and solutions near the center, in particular near the point ($\beta f = 1, (\gamma - \beta) f = 1$), decay rapidly.

The solutions near the line $(\gamma - \beta) f = 1$ are of special interest since on that line the servo action is of first order:

$$\epsilon_{n+2} - (1 - \beta f) \epsilon_{n+1} = (1 - f) \Delta r_t \quad (8)$$

The transient solution of (8) is

$$\epsilon_n = \epsilon_0 (1 - \beta f)^n$$

At the point $\beta f = 1, (\gamma - \beta) f = 1$, Eq. (2) becomes

$$\epsilon_{n+1} = (1 - f) r_t - \epsilon_n - B_n + d \quad (9)$$

Here, a sudden disturbance $\epsilon_n = \epsilon$ from the steady state corrects itself precisely in two steps: the error is first reversed, then nullified. This solution is not optimum, however, for two reasons: it is susceptible to spontaneous slow oscillations (of period about 8-10 steps) through such effects as backlash (dead band) and stick-slip friction, and the net mean-square error due to a stochastic forcing function of variance σ^2 is $2\sigma^2$, due to the error reversal.

A more favorable operating condition which combines the advantages of nearly full (one-step) correction of an initial error and smaller mean-square error is that near $\gamma = 1 - \beta, \beta < 1$. The equation is then

$$\epsilon_{n+1} = (1 - f) r_t + (1 - f + \beta f) \epsilon_n - \beta f B_n + d \quad (10)$$

The behavior of the drive-servo system during slew, acquisition, and tracking of a source is similar for each coordinate: The instantaneous error for each half-second interval is the difference, at the beginning of the interval, between the actual coordinate as measured by the encoder, and the requested coordinate provided to or calculated by the computer. If the error ϵ_n is greater than some multiple N of the slew rate times 1/2 second (say $N=4$), the telescope is driven at the slew rate and the bias B_n is set to zero. As the actual coordinate approaches the requested one, a gradual speed reduction is imposed such that the speed decreases linearly with the error and would go to zero at zero error (Fig. 26). (Effectively, the motor speed vs. error is divided by N .) However, if the error is less than $1/N$ of the slew rate times 1/2 sec., the speed - vs. - error is restored to its full value. Thus the servo loop possesses its one-step nominal error correction potentiality over a reduced range. In this inner, tracking range the bias is unclamped from zero and allowed to increment normally.

Because of the small value of β , the initial acquisition results in an error approximately equal to that given by Eq. (3), which slowly diminishes to zero as the bias builds up to the value given by Eq. (4). The time constant for this is approximately $B_{ss}/\epsilon_{ss} = \gamma/\beta$ steps.

Once the bias has reached its steady-state value, further errors may arise either directly, (e.g. through wind forces), or indirectly through a change in tracking rate r_t .

The response of the system to an isolated error ϵ_0 is

$$\epsilon_n = \epsilon_0 \frac{[\theta_2^{n+1} - \theta_1^{n+1} - \theta_2^n + \theta_1^n]}{(\theta_2 - \theta_1)}$$

The sum of the squares of this sequence of errors is

$$\sum_0^{\infty} \epsilon_n^2 = 2 \epsilon_0^2 / (1 + \theta_1)(1 + \theta_2)(1 - \theta_1 \theta_2) \quad (|\theta_1|, |\theta_2| < 1)$$

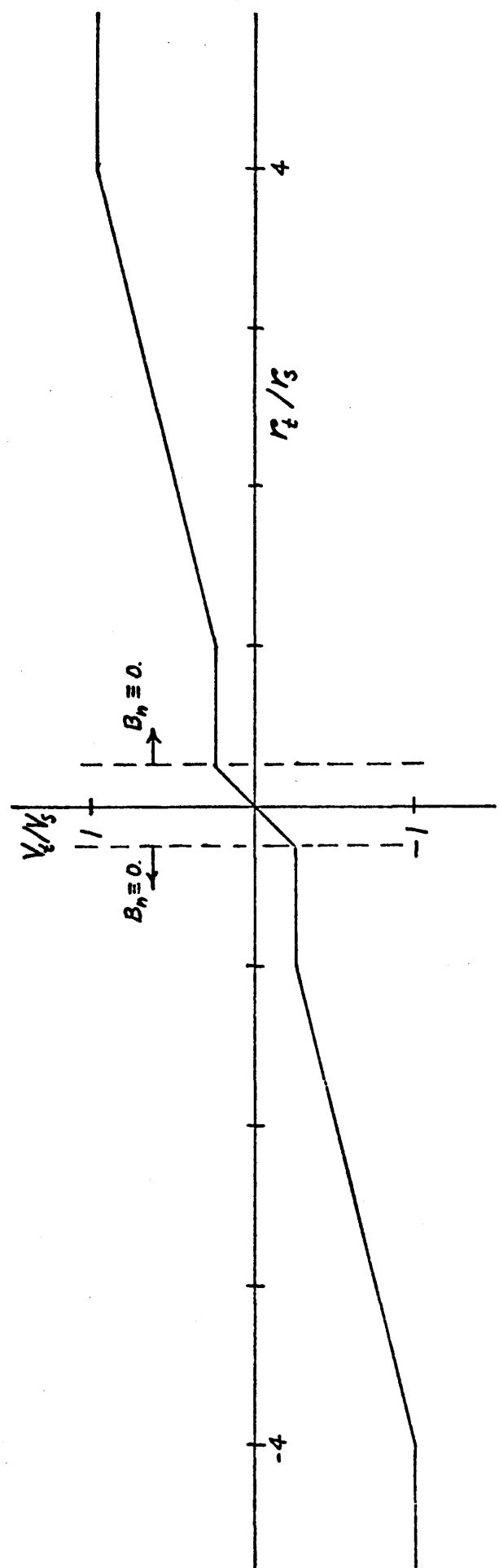


Figure 26: Servo drive voltage versus the nominal computed tracking rate r_t . this characteristic, which is a part of the software servo loop, slows the telescope gradually from its slew rate r to its tracking rate $r < r_s$, and yet maintains a "stiff" response for small tracking rates (up to 5' per second). The bias is forced to zero outside the steep innermost region.

Therefore, the response to an uncorrelated series of errors of variance σ^2 is such as to increase the variance by a factor $2/(1+\theta_1)(1+\theta_2)(1-\theta_1\theta_2)$, or equivalently, $2/(4-2\gamma f+\beta f)(\gamma-\beta)f$. For $\gamma=1, \beta=0.2, f=1$, this factor is about 1.12, a negligible increase over the variance of the error series itself.

Fig. 27 shows the transient response of the servo to three kinds of forcing terms:

- a) a sudden change in tracking rate, as might occur in the course of a raster scan;
- b) a one-time "spike" in tracking rate, as would result from the sudden introduction of a fixed pointing offset.
- c) a single pointing error, as discussed previously.

2. Absolute pointing accuracy; level system.

When properly adjusted, the drive servo-system follows a designated point in the sky with an rms error of one or two arc seconds, as measured by the difference between the desired and the actual encoder readings. However, without special precautions, the absolute pointing accuracy is generally not better than 5 - 10 arc seconds rms at the present preliminary stage. Some of the factors which affect the absolute pointing accuracy are

- 1) Encoder zero errors
- 2) Latitude, longitude, and time errors
- 3) Non-orthogonality of elevation and azimuth axes
- 4) Elastic "sag" of the dish and feed system
- 5) Regular and irregular changes in azimuth axis tilt
- 6) Thermal distortion of the dish and mount

Of these, 1) - 4) are relatively stable, 5) is measured and corrected for in real time, and 6) is minimized by thermal insulation of the most sensitive mount parts and by working at night. Following are comments on the individual factors.

Figure 27: Servo response to various unit forcing terms. Upper curves: response to a unit error at step 0, for two values of γ and three values of f . The initial error is reduced at once by about a factor of five, and remains less than 1/10 its original value after about six steps (3 sec). Lower right: response to a unit offset. Note that for $f=1$, the response is exact in one step. As expected, the initial error in the offset is essentially due to the departure of the motor speed factor from unity. It is relatively easy to maintain f in the range $0.9 < f < 1.1$. Lower left: response to a unit rate change. Here, also, the response is exact for $f = 1$ and departs from this condition in proportion to $f-1$.

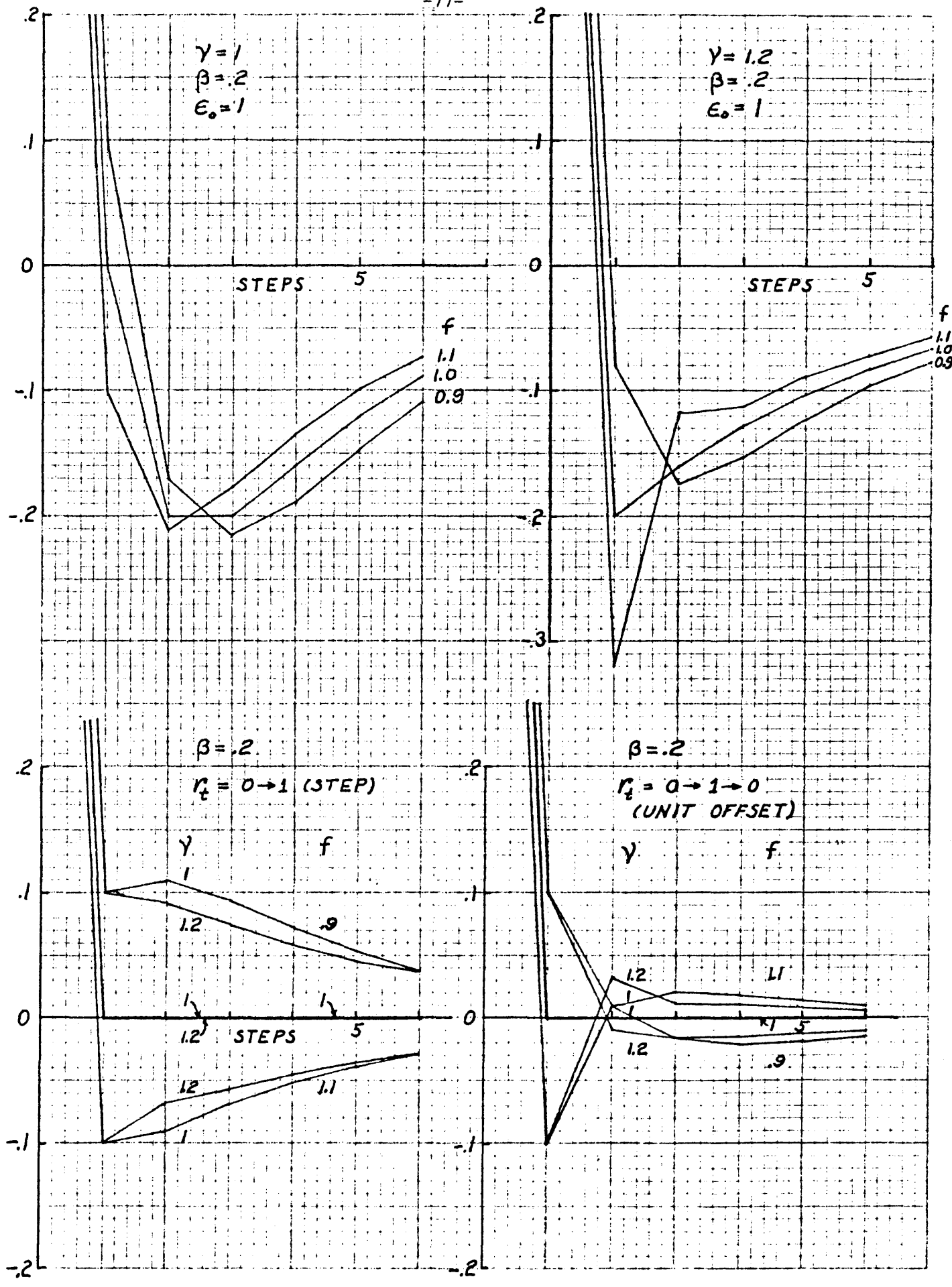


Figure 27

1) The zenith angle encoder zero reading is determined with the help of the measurement tower (p. 63). A position transducer senses the local height of the dish surface near the dish edge as the telescope is rotated about its azimuth axis. The zenith angle of the dish is adjusted so as to remove the fundamental $\cos(AZ)$ term in the transducer record and the corresponding zenith angle encoder reading is taken as the zero value. Feed-leg centering and subreflector collimation are carried out using the measuring tower in a similar way. The accuracy attained is about 2-4 arc seconds.

2) Situated as it is between two major mountain ranges - the Sierra Nevada and the Inyos - the deviation of local gravity from the nominal vertical is significant, probably at least 10 arc seconds. This is treated as a fixed deviation of the azimuth axis from vertical. Latitude, longitude, and time errors are taken as zero when the sidereal clock registers local sidereal time based upon UTC and reduced to the nominal longitude of the telescope.

3) The elevation and azimuth axes were adjusted mechanically to be orthogonal within about 5 arc sec.

4) The elastic sag of the dish and feed can be computed using the dish deformation computer model, and can also be evaluated experimentally by least-squares fitting to pointing data. The former method is used to compute the detailed deformation of the dish (for purposes of correction to zero error at 45° zenith angle), but the latter method is used to evaluate the overall effect.

5) A major effect in the pointing error budget is that caused by azimuth axis tilt away from the vertical. Several sources of axis tilt are identifiable:

- a) Secular tilting due to settling of the mount base
- b) Diurnal and other short-term effects due to thermal distortion of the mount base by sunlight, warm or cold air currents, etc.
- c) Axis wobble as a function of azimuth due to non-circularity of the top cone bearing ring (p. 60)
- d) Axis tilt as a function of zenith angle due to unbalance of the elevation axis, dish, and counterweights.
- e) Transient tilts due to wind forces.

All of the above are measurable (in the aggregate) and correctable in real time using a pair of sensitive electrolytic bubble-levels mounted inside the azimuth cone. These levels provide both a chart-record readout (Fig. 28 - see also page 8) and a computer-compatible analog voltage which is introduced directly into the pointing corrections. The sensitivity is more than adequate, and the zero stability is sufficient to give satisfactory pointing for at least a full day at a time. Re-establishment of the zero correction requires about fifteen minutes.

With the telescope in good mechanical adjustment, the residual misalignments are evaluated by six-parameter least-squares fitting to pointing-offset data for several sources distributed around the sky. The data consist either of radio sightings using the telescope itself with a suitable receiver, or of optical sightings using an auxiliary 10 cm refractor with a CCTV camera, rigidly fixed to the dish support frame. Radio data are of course preferable from the standpoint of directness but the notable dearth of strong "point" sources at 1 mm wavelength requires rather elaborate and time-consuming procedures to obtain sightings of the necessary precision. The small optical telescope, while still limited to 20 or so bright-star sources (without resorting to an integrating mode for the CCTV system) has definite advantages in the rapidity of obtaining data and in providing a directly visible image on the screen. This is particularly useful, for example, in observing the tracking behavior in the presence of wind since all error sources, both inside and outside the servo loops, contribute to the observed excursions.

Given at least 10 or 15 good sightings, the rms pointing error has been found to be as small as 6 arc seconds. This is probably not much greater than the best that can be attained with the present 20-bit (1.25 arc-sec) encoders, and in an unenclosed environment. There is reason to hope that more refined analysis of error sources, and more actual pointing experience, might reduce the rms to 3 arc seconds or so. If so, this would be a valuable improvement and would make feasible several observational programs which are otherwise only marginally possible.

Figure 28: Electrolytic-level azimuth axis tilt records. Solid curve: Forward-aft axis tilt; dashed curve: right-left axis tilt. Time-and tilt-angle-scales are indicated on the lower record. The mount was stowed at 0° zenith angle and at 180° azimuth ("forward" direction = south, "right" direction = west) during the above time. The records clearly show: the general sensitivity and stability of the level system; significant diurnal excursions due to solar heating of the mount base; the response of the mount base to wind speeds up to $30\text{-}40 \text{ km hr}^{-1}$ (18-19 Feb.).

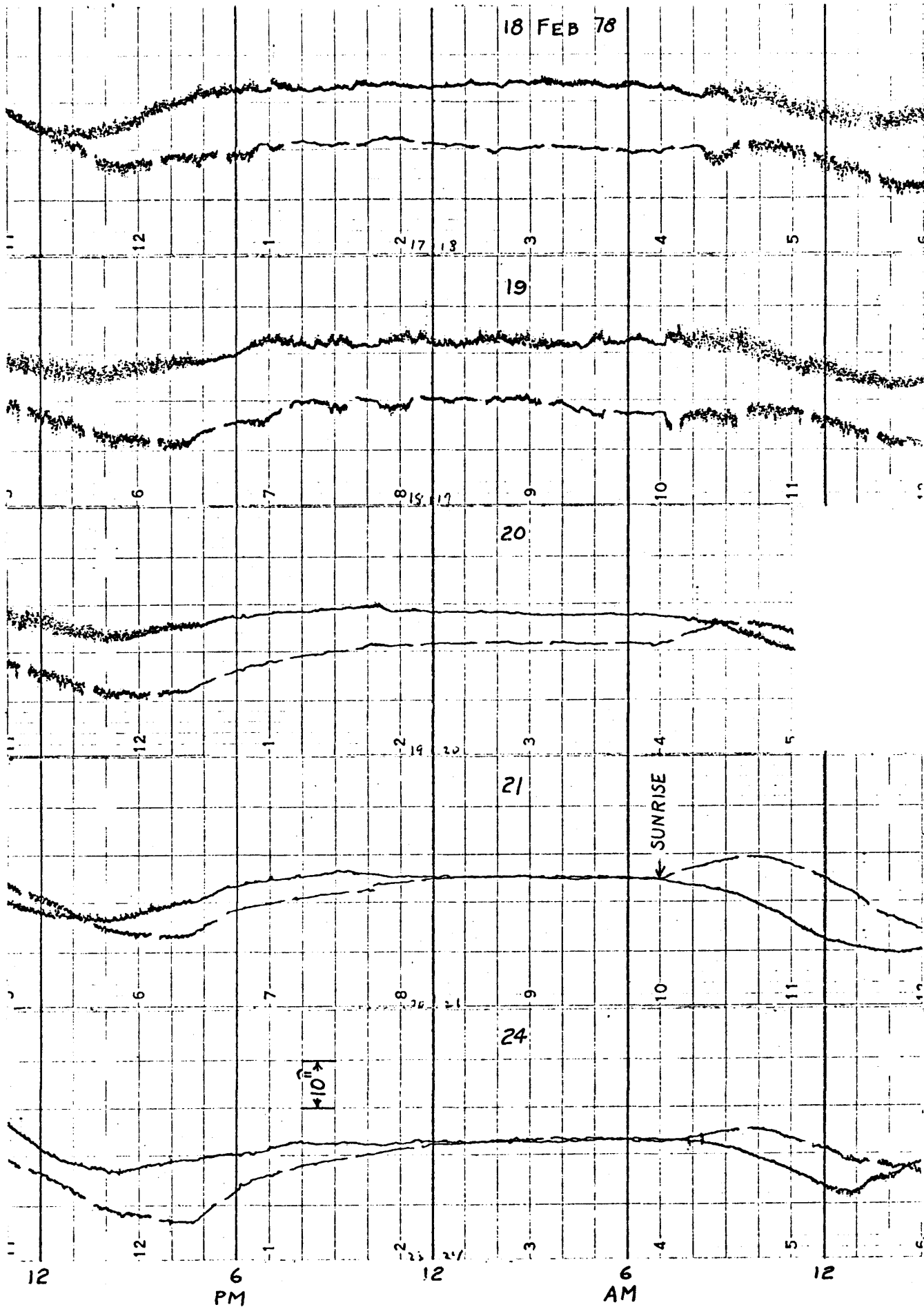


Figure 28

SUMMARY AND CONCLUSION

The 10-meter prototype telescope project served its purposes, which were to test and prove out certain new dish-fabrication techniques which seemed to promise a dramatic improvement in surface accuracy, and to design and fabricate a suitable, economical mounting for such a dish. It is fair to say that the prototype instrument has met, and has in many respects exceeded, the quite high performance goals that were originally set. When fully outfitted with the best available receivers, this telescope will surely become one of the most powerful instruments available for millimeter-and submillimeter astronomy.

The next phase of the overall project, now underway, is to build two more such instruments and to provide the means to operate these as a three-element millimeter-wave interferometer at OVRO. The second telescope will be in place in summer, 1978, and the third in summer, 1979. In each case, several weeks will be required to complete the assembly, wiring, and mechanical adjustment, and several months of quasi-operation for shake-down, alignment, and electronic outfitting. A current goal is to have seen fringes at 2.6 mm wavelength, with two instruments on a 50-meter baseline, before the end of 1979.

Another important related project, to be undertaken in 1979 or 1980, is to build an even more precise instrument, mechanically similar or identical to the first three but to be situated on a high, dry mountain site. This instrument will have a surface accuracy of 10 μm rms or perhaps even better, and is especially intended for submillimeter work down to 300 μm , where it will have unique capabilities. The dish for that instrument may be produced in 1979 as the third dish of the planned four; the mount is expected to be provided, under a challenge grant, by the Kresge Foundation.

This report is intended to describe the highlights of the project under which the prototype (now the first) 10-meter telescope was produced. Obviously, it is not a complete report. Numerous details of possible interest had to be omitted, but many of these can be (and have been) supplied to interested groups by special arrangement.

Acknowledgements

Any complex technical enterprise, even a relatively modest one like this, requires the substantial participation of many skilled persons and might not succeed at all without the essential contributions of a special few. Extending as it did over several years from concept to completion, the present project involved so many persons directly or indirectly, that it would be most difficult to acknowledge all the individuals who contributed significantly to it. The following partial list recognizes some of those who made special contributions.

Professional:

Engineering and Design:

Bruce Rule: Dish and mounting design concepts
Victor Ehr Gott: Mount design layout
Robert Lyon: Fabrication concepts and initial tooling
Walter Schaal: Detail design

Mechanical and Fabrication:

David Vail: Dish fabrication and technical supervision
Walter Schaal: Mount fabrication

Computer Hardware and Software:

Martin Ewing: Computer system concepts
H. Wayne Hammond: Computer operating system software
Barbara Zimmerman: FORTH Language software

Technical:

Joseph Lyvers: Prototype dish fabrication
Larry Van Stone: Prototype dish fabrication
Jeffrey Clark: DISH 1 fabrication and surface measurements

OVRO Staff:

Telescope Assembly, Wiring, and Adjustment:

O. Wayne Hutton: Mechanical and supervision
Chick O. Lackore: Mechanical and assembly
Ronald E. Allen: Electrical layout and wiring

Student Technicians:

John Bean:	3-meter dish and early 10-meter prototype parts
Raymond Waldo:	Prototype dish fabrication
Michael Norman:	Prototype dish fabrication
Donald Macglashen:	Prototype dish fabrication
Eric Tollestrup:	DISH 1 fabrication
Kurt Tollestrup:	DISH 1 fabrication
Robert Calvet:	DISH 1 and DISH 2 fabrication
Isabella Lewis:	DISH 2 fabrication
Norman Murray:	DISH 2 fabrication

Faculty and Research Investigators:

Co-investigators :

Alan Moffet:	Electrical system design
Gerry Neugebauer:	Infrared instrumentation

Research Investigators:

Thomas Phillips:	(Bell Laboratories) Receiver design and 1 millimeter measurements
Peter Wannier:	Receiver design and fabrication